A dual-VENC 4D Flow MRI Framework for Analysis of Subject-Specific Heterogeneous non-linear Vessel Deformation

Concannon J[1], Hynes N[2], McMullen M[3], Smyth E[3], Moerman K[1], McHugh PE[1], Sultan S[2], Karmonik C[4], McGarry JP[1]

[1] Biomedical Engineering, National University of Ireland Galway.

[2] Department of Vascular and Endovascular Surgery, National University of Ireland Galway.

[3] Department of Radiology, Galway Clinic, Doughiska, Galway, Ireland.

[4] MRI Core, Houston Methodist Debakey Heart and Vascular Center, Houston, TX, USA.

Corresponding Author: Patrick McGarry

Email: patrick.mcgarry@nuigalway.ie

Tel: +353 (0)91 493165

Abstract

Advancement of subject-specific *in-silico* medicine requires new imaging protocols tailored to specific anatomical features, paired with new constitutive model development based on structure/function relationships. In this study we develop a new dual-VENC 4D Flow MRI protocol that provides unprecedented spatial and temporal resolution of *in-vivo* aortic deformation. All previous dual-VENC 4D Flow MRI studies in the literature focus on an isolated segment of the aorta, which fail to capture the full spectrum of aortic heterogeneity that exists along the vessel length. The imaging protocol developed provides high sensitivity to all blood flow velocities throughout the entire cardiac cycle, overcoming the challenge of accurately measuring the highly unsteady non-uniform flow field in the aorta. Cross sectional area change, volumetric flow rate, and compliance are observed to decrease with distance from the heart, while pulse wave velocity is observed to increase. A non-linear aortic lumen pressure-area relationship is observed throughout the aorta, such that a high vessel compliance occurs during diastole, and a low vessel compliance occurs during systole. This suggests that a single value of compliance may not accurately represent vessel behaviour during a cardiac cycle *in-vivo*. This high-resolution MRI data provides key information on the spatial variation in non-linear aortic compliance which can significantly advance the state-of-the-art of *in-silico* diagnostic techniques for the human aorta.

Keywords: dual-VENC 4D Flow MRI; heterogeneous compliance, pulse wave velocity; non-linear compliance.

1 Introduction

Of the 97,000 km of blood vessels in the human body, the near-metre long segment connecting the left ventricle to the periphery, known as the aorta, is the most important. Diseases affecting the aorta such as aneurysm and dissection have long been documented, but still today remain difficult to treat. According to the Centre for Disease Control and Prevention, an average of 47,000 deaths each year in the United States are attributed to diseases of the aorta and its branches (excluding carotid and coronary disease). This exceeds the number of annual deaths due to breast cancer, pancreatic cancer, colon cancer and prostate cancer [1].

Patients undergoing surgery of the aorta have two main treatment options: open surgical repair (OSR); or endovascular aortic repair (EVAR). The introduction of EVAR in the early 1990s was fuelled by the need for a less invasive treatment option for co-morbid patients and poor outcomes following OSR. In the quarter-century since its introduction, EVAR has shown superiority over OSR in the short-term, where studies continue to report mortality rates from 14% to 45% in the first 30 days post-OSR [2], [3], but no significant benefits are apparent for EVAR patients in the long-term [4].

As the first thoracic endovascular aortic repair (TEVAR) graft only received FDA approval in 2005 [5], long-term results are only now coming to light. A number of studies have reported high levels of cardiac complications following TEVAR, where Conrad [6] reports 34% mortality due to cardiac events in thoracic aortic aneurysms (TAA), while a study by Bischoff [7] reports 30% cardiac mortality for a larger TAA cohort. A recent study by Concannon [8] reports that, from a cohort of 151 patients with thoracoabdominal aortic aneurysms (TAAA), 39% of total deaths were due to cardiac failure. Notably, all deaths due to new onset cardiac complications were in patients who underwent stenting of the supradiaphragmatic aorta. Altogether, these results suggest a dependence of post-operative cardiac outcomes on the location of stent deployment in the aorta.

A detailed biomechanical investigation of the influence of stent deployment on aortic deformation, haemodynamics, and pulse wave velocity (PWV) is required to uncover the mechanisms that cause cardiac complications post-TEVAR. As an important first step in this process, we propose a non-invasive 4D Flow MRI protocol to accurately characterise spatial variations in biomechanical behaviour throughout the entire aorta, in addition to dynamic variations throughout a cardiac cycle. The ability to characterise spatially dependent vessel geometry and deformation, blood flow patterns, and PWV will potentially guide the selection

of stent-graft design and position in EVAR procedures in order to minimise the risk of cardiac complications post-intervention. An increased PWV has been established as a strong risk factor for cardiac events, independent of traditional risk factors such as smoking, hypertension and diabetes mellitus [9]. The ability to accurately determine the spatially non-uniform PWV throughout the entire aorta, both pre- and post-intervention, could potentially provide new insights.

The increase in clinical acceptance of EVAR has resulted in a reduction in the number of primary OSR cases [10], and a consequent reduction in the availability of tissue samples for *in-vitro* biomechanical testing. Moreover, surgically excised tissue often consists of a small portion (approximately 1 cm^2) of the aorta, presenting significant challenges in terms of bi-axial mechanical testing [11]. Therefore, *in-vitro* testing of excised tissue does not present a viable methodology to accurately determine the detailed spatial variations in compliance and PVW in a patient-specific aorta. Alternative approaches of combined medical imaging and computational analysis (finite element (FE) and computational fluid dynamics (CFD) modelling) to determine biomechanical properties non-invasively are highly promising, particularly in light of recent advances in medical imaging technology and computational capability.

Of the few studies that attempt to investigate the biomechanics of the aorta, its heterogeneity has been reasonably well established in animals through *ex-vivo* testing of the excised vessel [12], [13]. Previous *in-vivo* analyses of the human aorta have focused on limited isolated segments, such as the thoracic [14] or abdominal aorta [15], which fail to provide the necessary anatomical coverage to capture the true heterogeneity and therefore cannot be taken to represent the entire vessel. Due to the lack of reliable and detailed information on the heterogeneity of the aorta, computational models have typically assumed that the wall stiffness is spatially uniform throughout the vessel [16]–[19]. An improved robust methodology to non-invasively characterise patient-specific spatial variation in aortic PWV and compliance throughout the cardiac cycle has the potential to provide accurate heterogeneous material properties for computational models, leading to significant improvements in EVAR device design, and subsequently, postoperative outcomes.

In-silico tools are being considered as possible replacements for animal and human experimentation and the pre-clinical assessment [20]. Advancement of subject-specific *in-silico* medicine requires new imaging protocols tailored to specific anatomical features, paired with new constitutive model development based on structure/function relationships. In this study a dual-VENC 4D Flow MRI protocol is developed to achieve accurate

measurement of the dynamically changing flow velocity field and lumen area throughout the entire cardiac cycle and the entire aorta. To the best of our knowledge, no previous medical imaging paper has reported such detailed spatial and temporal characterisation of the human aorta. To date, 12 aortic dual-VENC 4D Flow MRI studies exist in the literature, 4 of which pertain to phantom geometries [21]–[24], while the remainder are focused on a single isolated segment of the aorta such as the ascending thoracic [25]–[31]. A nonlinear relationship between lumen area and pressure is observed *in-vivo* over the duration of a cardiac cycle throughout the entire aorta, suggesting that aortic biomechanics may not be accurately characterised by a single value compliance coefficient, as commonly assumed [32]–[34]. Furthermore, our detailed *in-vivo* measurements reveal that the lumen pressure-area relationship, and PWV are highly heterogeneous along the aortic length.

2 Methodology

In this paper a protocol is proposed to evaluate patient-specific haemodynamics and lumen deformation along the entire human aorta, and throughout the entire cardiac cycle, using phase-contrast magnetic resonance (PC-MRI) principles (specifically, 4D Flow MRI). Further details of the applications and potential uses of 4D Flow MRI can be found in: [35]–[40]. Generally, with the aim of assessing anatomical structures, it is the magnitude of the local spin magnetization vector that is used in the creation of typical MR images. However, important information regarding the movement of hydrogen protons is encoded in the phase of this vector. In the field of PC-MRI, such information is exploited to determine the flow velocity of targeted protons. A brief summary of the theoretical background to PC-MRI is presented in Section 2.1 to motivate the protocol proposed in this paper. Further details pertaining to spin dynamics and velocity encoding sensitization can be found in Appendix A.

2.1 Theoretical background

In this section we provide a brief overview of the key theory and equations that motivate the dual-VENC protocol proposed in Section 2.2. The theoretical physics underlying MRI is extensively outlined in literature, e.g. [41]–[43]. In summary, MRI is a phase-sensitive modality that encodes information regarding the velocity of the targeted protons into the detected signal. The velocity is proportional to the phase of the local transverse magnetization vector. In the remainder of this paper the term *spins* is used to refer to a finite group of protons within a given volume. In Figure 1, cranial flow (in the positive z-direction) is indicated in red on the FH image in the ascending thoracic aorta. The flow direction is in the negative z-direction in the descending aorta, as indicated by blue in the FH image. In the AP

image, posterior flow can be seen traversing the apex of the aortic arch while anterior flow is indicated by blue as blood leaves the left ventricle into the ascending thoracic aorta. Similarly, flow sensitization is seen with the RL image although velocity encoding is less obvious in the RL direction upon viewing a sagittal plane.

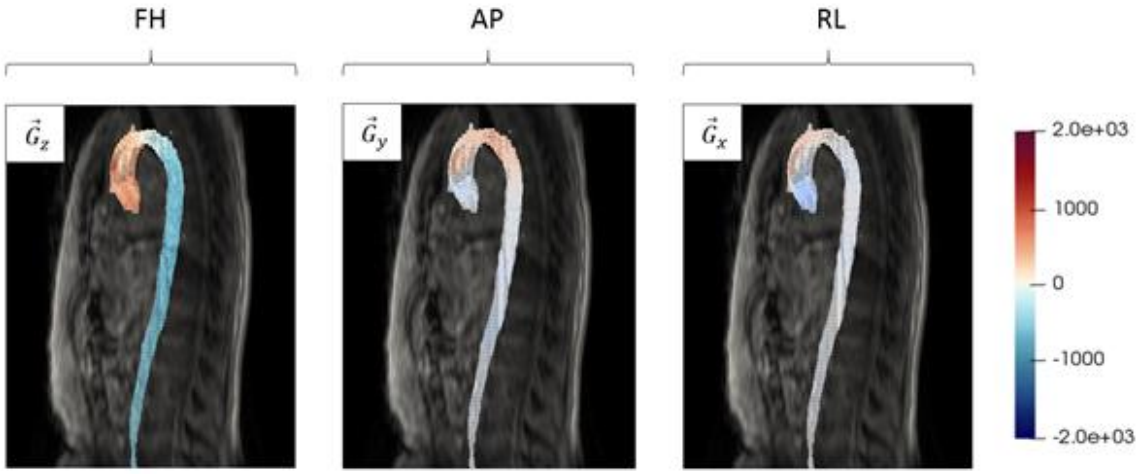

Figure 1: Sensitization along the three principle orthogonal directions, where FH, AP and RL indicate Foot-Head, Antero-Posterior and Right-Left, respectively (also referred to as the z, y, and x components of a Cartesian coordinate system).

Due to the orthogonality of the chosen velocity encoding directions, the velocity magnitude of a given voxel is simply given as:

$$|\vec{v}| = \sqrt{\vec{v}_x^2 + \vec{v}_y^2 + \vec{v}_z^2} \tag{1}$$

Defining ΔT as the period for which a magnetic field gradient ($\vec{G}$) is switched on, regardless of its polarization, the first moment M_1 of the bipolar gradient can be calculated directly as:

$$M_1 = \int_{T_0}^{T_0+\Delta T} +\vec{G}_i t \, dt + \int_{T_1}^{T_1+\Delta T} -\vec{G}_i t \, dt = \vec{G}_i T_1 \Delta T \tag{2}$$

Recognising that $\vec{G}_i \Delta T$ is equal to the area of an individual gradient lobe A and T is the time from T_0 to the time at the beginning of the second gradient lobe T_1, an instantaneous flip of the polarization of $\vec{G}$ [31] gives:

$$M_1 = AT = \vec{G}_i T^2 \quad ; \quad \Delta M_1 = 2\vec{G}_i T^2 \tag{3}$$

The velocity sensitization is therefore dependent upon the strength of $\vec{G}$ and the time T over which it is active, such that

$$\vec{v} = \frac{\Delta\emptyset}{2\gamma\vec{G}_i T^2} \quad (4)$$

Equation 4 dictates how the scanner can sensitize to specific fluid velocities. For example, reducing the velocity encoding coefficient (VENC) from 200 cm/s to 50 cm/s requires a four-fold increase in the strength of $\vec{G}$, or an increase in the time over which it is activated. Thus, it is preferable that the strength of the magnetic field gradient be increased to achieve a reduction in velocity sensitization, instead of increasing T necessitating unfeasibly long scan times.

2.2 Proposed dual-VENC protocol for complete characterisation of aortic flow

Maximal sensitivity is obtained for spins moving at a velocity equal to the specified VENC value. This presents a particular challenge for determination of blood flow patterns in the aorta where flow is highly unsteady (temporally varying) and non-uniform (spatially varying). For example, a VENC of 200 cm/s, may provide a suitable level of sensitivity to determine the high velocity blood flow patterns in the aortic arch during systole. However, such a VENC value is not suitable during the diastolic phase, where the fluid velocity is considerably lower. In fact, in using a VENC of 200 cm/s, low velocity blood flow during diastole cannot be distinguished from static tissue and the lumen of the aorta cannot be reliably identified. A reduced VENC is required to achieve sufficient resolution of the flow field during diastole.

Of course, such a low VENC is not suitable for systolic flow velocities; any fluid velocity greater than VENC will be misrepresented and aliased, as described elsewhere [44]–[46]. In an attempt to overcome this issue, previous studies have proposed phase unwrapping algorithms to estimate velocities higher than VENC. However, significant errors have been reported for such techniques, in addition to increased post-processing time [47]–[49].

The dual-VENC protocol proposed in this study generates a composite dataset, with a high-VENC of 200 cm/s targeted to systole and a low-VENC of 50 cm/s targeted to diastole. As the only difference between our two datasets is the velocity sensitization, accurate velocity field measurement and lumen boundary isolation can be performed for each phase and plane throughout the entire cardiac cycle, all the while keeping acquisition parameters within the bounds specified in the most recent *4D Flow MRI expert consensus statement* [50].

If the velocity of any pixel in an arbitrary plane of interest is greater than our low-VENC value (50 cm/s) we use the high-VENC matrix to calculate the cross-sectional-area and volumetric flow rate; otherwise, we use the corresponding low-VENC matrix. This approach negates the need for phase unwrapping techniques and provides greater accuracy in flow quantification in areas where the fluid velocity is low than single high-VENC acquisitions.

2.3 Imaging parameters

The current study was approved by the institutional review board (Research Assessment Group (RAGp), Galway Clinic) and was conducted on a healthy 25-year-old male with a normotensive blood pressure measurement of 117/73 mmHg and a heart rate of 60 bpm. The subject was placed in a Philips Ingenia 3T MRI scanner (Philips Medical Systems, Best, Netherlands) and a 4-lead ECG system was placed on the chest with retrospective synchronization to the scanner to image according to specific phases of the subjects' cardiac cycle. A non-contrast RF-Spoiled Gradient Echo pulse sequence was employed in order to capture a sufficient number of heart phases under free-breathing conditions. The field of view was set to encompass the entire aorta. The longitudinal (FH) boundaries spanned from above the level of the aortic arch to distal to the common iliac bifurcation, while the lateral (AP) and (RL) bounds enclosed the breadth and width of the subject respectively. The frequency encoding direction was set to AP to reduce artefact from respiratory motion. Important scan parameters are as follows: repetition time (TR) = 3.1 ms, echo time (TE) = 1.9 ms, Flip Angle = 8°, cardiac phases = 20, temporal resolution = 50 ms, isotropic in-plane resolution = 1 mm, slice thickness = 4 mm, VENC = 200 cm/s and 50 cm/s. VENC scouts were ran to obtain the minimum high-VENC value to prevent aliasing and optimize Signal to Noise Ratio (SNR), while a 4 mm slice thickness was used to limit scanning time. The scan time for a VENC of 200 cm/s was 4 minutes, and 8 minutes for a VENC of 50 cm/s. In the case of the latter, the TR was increased to 10 ms to allow sufficient down-time for the gradient coils to prevent excessive overheating. A balanced four-point encoding scheme was used, further details of which can be found in [51].

2.4 Postprocessing

All data was processed using in-house developed C++, Python and MATLAB code. Data processing was performed on an Intel Core i7 CPU with 16GB DDR3 RAM. Post-processing time for the dual-VENC dataset was approximately 20 minutes. Raw MRI data files were sorted according to their encoding direction using RadiAnt DICOM Viewer (v4.2.1, Medixant, Poznan, Poland) and subsequently organised according to the time-point in the

cardiac cycle using a custom Image J plugin (Figure 2(a)). ParaView (5.4.1, www.paraview.org) visualisation software served as the platform for reading the image data for each encoding direction, developing voxel associativity and subsequent calculation of local velocity magnitudes $|\vec{v}|(x, y, z, t)$ as illustrated in Figure 2(b). It is necessary to ensure that observational planes are orthogonal to the mean direction of blood flow when attempting to characterize lumen deformations and volumetric flow rates due to the onset of a pressure pulse. A centreline detection algorithm was developed to ensure such requirements were fulfilled as shown in Figure 2(c), where the centreline is defined as the centroid of the aortic flow domain.

Analyses were performed at 10 planes along the aorta (Figure 2(d)), ranging from Plane 1 distal to the sinus of Valsalva to Plane 10 immediately proximal to the common iliac bifurcation, with an average section spacing along the centreline of 50 mm. Each time-point for each plane in both VENC datasets was then exported for all further postprocessing in MATLAB (R2017b, MathWorks Inc., Natick, MA, USA). A bicubic interpolation algorithm is employed in order to attain further clarity for aortic lumen edge detection. A series of cubic splines were fit to the intensity values of individual pixels along both the x and y dimensions in a given plane (Figure 2(e)) and the grid density was increased to 0.5 x 0.5 mm in-plane spatial resolution. Figure 2(f) (i) and (ii) highlight in-plane pixel data pre- and post-interpolation.

At this point, each velocity magnitude image is masked by the square of the corresponding magnitude (anatomical) image (Figure 2(f) (iii)) in order to create a PC-MRA matrix according to methods described in [52]. Using each PC-MRA image, the boundary of the fluid domain is isolated for each plane and phase of interest to determine the lumen area as a function of space and time based on a custom-built segmentation algorithm. Using the high-VENC velocity matrix, if the velocity of any pixel is greater than the low-VENC value (50 cm/s) we use this matrix to calculate the cross-sectional-area and volumetric flow rate. Otherwise, the corresponding low-VENC matrix is used. The composite data set generated by the dual-VENC protocol eliminates the need for any phase unwrapping techniques.

For each of the 10 planes analysed, the percentage cross-sectional-area change ($\Delta\hat{A}$) is defined according to $(A_{sys} - A_{dia})/A_{dia}$, where subscripts '*sys*' and '*dia*' represent systole and diastole respectively. After isolating the aortic lumen from surrounding structures, streamlines and flow vectors can be plotted as shown in Figure 2(g). The integral of the velocity within the boundary of the aortic lumen provides the instantaneous volumetric flow

rate (Q) as shown in Figure 2(h). Finally, the local PWV at each plane is calculated according to the QA method described in Vulliémoz [41] and shown in Figure 2(i), where PWV is defined as the coefficient of proportionality between Q (blue) and CSA (red) bound by the systolic upstroke of the cardiac cycle. Additionally, spatial variance in PWV is calculated using the time-to-peak (TTP) method described in [54], where in this case the wave speed is defined as $\Delta z/\Delta t$, where Δz is the distance along the vessel centreline between regions of interest and Δt is the time lag between flow peaks for the thoracic and abdominal aortic segments in this case.

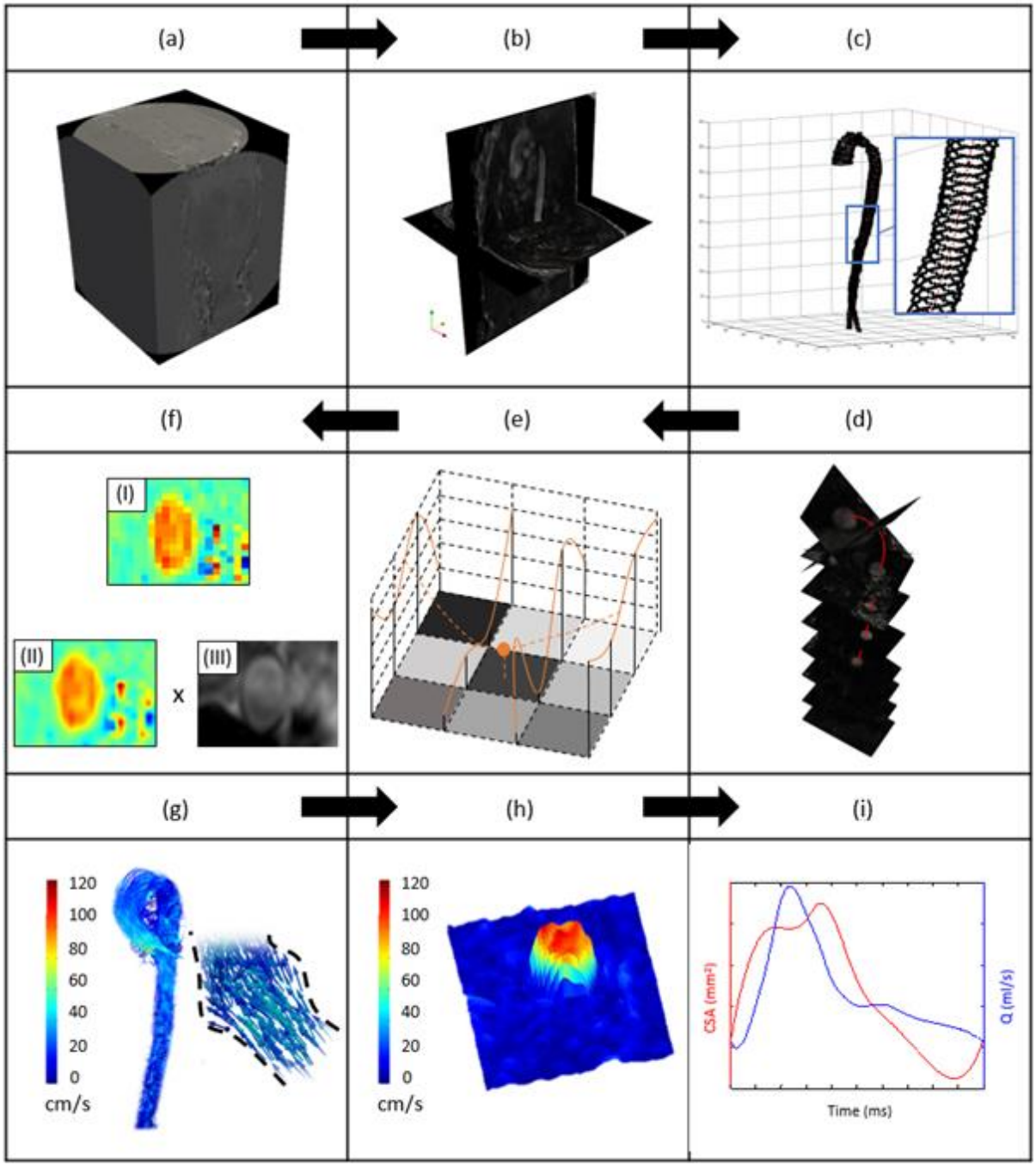

Figure 2: Basic overview of postprocessing steps. (a) Raw MRI volume of interest (b) velocity magnitude calculation using equation 14 from each encoding direction. (c) Centreline detection algorithm and (d) centreline highlighted in red with 10 orthogonal observational planes created normal to the mean direction of flow along entire aorta. (e) Bicubic interpolation process to increase in-plane spatial resolution. (f) Pre- (I) and Post- (II) interpolation, final matrix is multiplied by magnitude data (III) to form a PC-MRA image. (g) Streamlines plotted at 200ms into cardiac cycle. (h) Volumetric flow rate through an observational plane in the descending thoracic aorta during the systolic upstroke. (i) Flow (blue) and CSA (red) as a function of time in cardiac cycle, where the constant of proportionality can be used to calculate pulse wave velocity.

2.5 Compliance

To estimate local vessel compliance, the pressure must be estimated throughout the cardiac cycle at the location in question. The clinical definition of vessel compliance is typically given as $\Delta CSA/\Delta P$ during a cardiac cycle. Typically, vessel compliance is reported as a single value [34], [55], [56] as only the systolic (SBP) and diastolic pressures (DBP) are recorded. However, it is trivial to demonstrate that, even for the simplistic thin-walled linear-elastic cylindrical vessel undergoing infinitesimal deformation, a linear relationship does not exist between ΔP and ΔCSA and therefore a single value of local compliance cannot be identified. Moreover, the well-established non-linear material behaviour of arterial tissue, e.g. [57]–[59], further invalidates the concept of a single value of compliance. By considering the entire blood pressure waveform, we investigate the time-dependence in local compliance along the length of the aorta.

As local variations in pressure are not directly measured, we consider four methodologies for estimation of time-dependent blood pressure throughout the aorta: Firstly, a generic central aortic blood pressure curve was scaled to the subject's cardiac cycle time, SBP and DBP (Figure 4(a)). This pressure-time relationship is applied to each plane in the aorta. Secondly, setting the aortic blood pressure waveform from method (a) to Plane 5, we employ the unsteady Bernoulli equation to calculate the blood pressure waveform at discrete proximal and distal planes (Figure 4(b)). Beginning with the Navier-Stokes equation;

$$\rho\left[\frac{\partial\vec{v}}{\partial \mathrm{t}}+(\vec{v}\cdot\nabla)\vec{v}\right]=-\nabla P+\rho\vec{g}+\mu\nabla^2\vec{v} \tag{5}$$

and assuming viscous effects contribute little to pressure differential compared to transient and convective terms as shown by [60], the last term in equation 5 goes to zero and we obtain the Euler equation. Multiplying by an infinitesimal increment dz along a streamline, such that dz is parallel to the mean velocity direction $\vec{v}$ gives

$$\rho\left[\frac{\partial\vec{v}}{\partial \mathrm{t}}+(\vec{v}\cdot\nabla)\vec{v}\right]\cdot dz=-\nabla P\cdot dz+\rho\vec{g}\cdot dz \tag{6}$$

Integrating between two arbitrary points (*Point 1* and *Point 2*) along a streamline yields

$$\int_1^2 \rho\frac{\partial\vec{v}}{\partial \mathrm{t}}dz+\frac{1}{2}\rho({v_2}^2-{v_1}^2)=-(P_2-P_1)-\rho\vec{g}(z_2-z_1) \tag{7}$$

where the first term on the left in equation 7 contains the integral of the local acceleration of a fluid particle along a streamline between *Point 1* and *Point 2*. ρ is the fluid density, P is the pressure, and $\vec{v}$ is the fluid velocity. We neglect the last term on the right-hand side as the subject is in the supine position in the scanner and hence the change in elevation along the vessel Δz can be taken as zero.

Thirdly, we investigate a piecewise approach of determining the aortic blood pressure waveform from PC-MRI data and non-invasive brachial blood pressure measurements (Figure 4(c)). The approach is described in detail in [61]. Briefly, the method makes use of the water hammer equation for the systolic upstroke phase of the cardiac cycle according to:

$$\Delta P=\rho\cdot PWV\cdot\Delta v \tag{8}$$

where P is pressure, ρ is density and v is blood velocity. A diastolic decay function driven by time constant τ is utilized for the phase between aortic valve closure and re-opening where:

$$P(t)=P_0\cdot e^{-\frac{t}{\tau}} \tag{9}$$

Finally, the systolic peak is approximated by a second-order polynomial which satisfies continuity and produces the prescribed mean arterial pressure (MAP).

Lastly, we perform a patient specific CFD simulation that solves for the pressure gradient at the ascending and abdominal aortic levels. A finite element mesh was generated by sweeping surface elements along the aortic centreline through each of the 10 planes analysed previously, using MATLAB (R2017b, MathWorks Inc., Natick, MA, USA) and GIBBON [62] (Figure 3). The inlet and outlet faces were closed off and the fluid domain was then filled with tetrahedral elements. A parabolic velocity profile derived directly from the MRI data at the aortic root was prescribed at the inlet. The outlet boundary condition consisted of a resistance (R) of 1.5e+08Pa s m^{-3}, representing downstream vasculature. The no-slip condition was prescribed at the lumen boundary of the aorta, while fluid back-flow and tangential stabilization (β=1) was defined at the outlet to deal with flow reversal and

increase stability of the solution ([63]). Blood was modelled as a Non-Newtonian Carreau fluid ($\mu_0 = 0.056; \mu_{inf} = 0.003; \lambda = 3.3s; n = 0.36$), with a density of 1060 kg/m^3. The resultant pressure waveforms for both the ascending thoracic and distal abdominal aorta are shown in Figure 4(d) below. The corresponding area versus pressure graphs are shown for each method in Figure 10(a), Figure 10(b), Figure 10(c), and Figure 10(d) respectively.

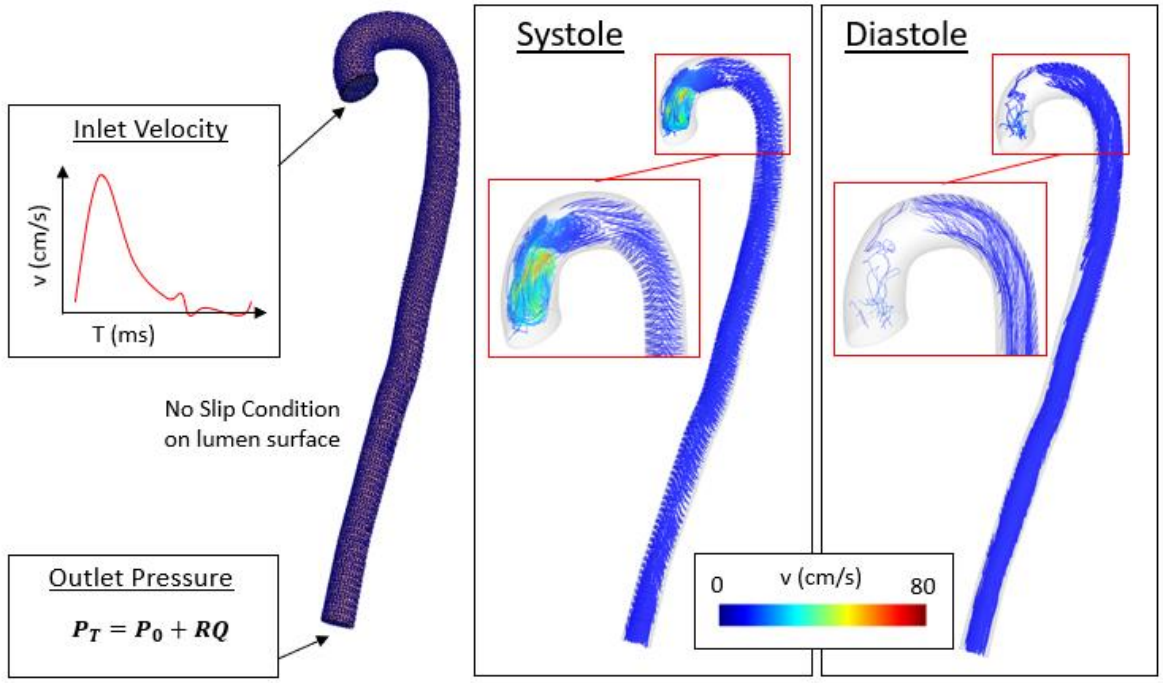

Figure 3: Method (d), CFD analysis using FEBio for the estimation of the pressure waveform in the ascending thoracic and distal abdominal aorta. Inlet Velocity waveforms are prescribed according to the mean velocities determined at the aortic root directly from the 4D Flow MRI data, while the total pressure (PT) at the outlet a function of the computed outflow and the peripheral resistance (R). Velocity streamlines are also plotted at diastole and systole highlighting the unsteady and non-uniform nature of aortic blood flow.

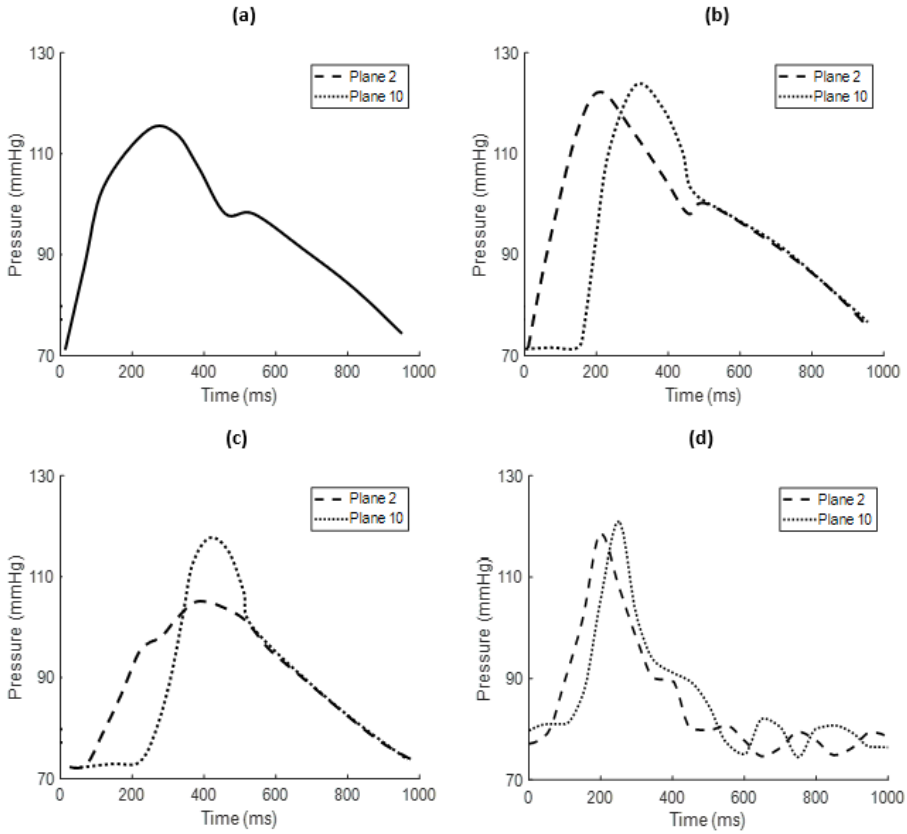

Figure 4: Pressure boundary conditions applied to calculate local aortic compliance. (a) Uniform; (b) Unsteady Bernoulli; (c) Piecewise; (d) CFD.

3 Results

3.1 Dual-VENC protocol for complete characterisation of aortic flow

We employ PC-MRI principles to capture both the deformation and haemodynamics of the entire aorta. The proposed dual-VENC protocol provides high sensitivity to all blood flow velocities throughout the entire cardiac cycle, overcoming the challenge of accurately measuring the highly unsteady non-uniform flow field in the aorta. A single high-VENC approach, while providing accurate measurements of high velocities during systole, was found to have insufficient resolution at low velocities to differentiate blood flow during diastole from the surrounding static tissue; this observation has been previously reported [25], [39], [64]. Consequently, the lumen geometry cannot be accurately determined in any region of the aorta during diastole, as clearly illustrated in Figure 5(a) (only the high velocity flow in thoracic aorta at a time-point of 200 ms (systole) is accurately measured). An inability to accurately determine the lumen geometry and velocity field in the entire aorta for the entire cardiac cycle prohibits the determination of clinically relevant quantities such as cross-sectional-area, aortic compliance, volumetric flow rate and PWV. As discussed in Section

2.2, a single acquisition low-VENC will not provide accurate measurement of high velocities during systole due to phase wrapping. This is evident in Figure 5(a), where the high velocities at 200 ms are significantly under-predicted by the low-VENC acquisition, compared to the high-VENC that is specifically sensitized for accurate measurement during systole. However, flow velocities and the flow domain are determined with greater accuracy at all other time-points (0, 500, 700 and 900 ms) using a low-VENC, in contrast to the high-VENC measurements where flow is indistinguishable from the noise associated with surrounding static tissue. As the velocity to noise ratio (VNR) is proportional to the velocity and inversely proportional to the VENC, comparably lower velocities (such as those in diastole) are measured with reduced accuracy [25], [65], [66]. Both phantom [67] and *in-vivo* [65] studies have shown that a dual VENC approach results in a more accurate flow quantification than single VENC acquisitions. Figure 5(b) further highlights this motivation for a dual-VENC approach. At 200 ms (top row), high-VENC accurately represents the fluid domain for the thoracic plane (indicated in red), whereas velocity aliasing is evident in low-VENC. In fact, some velocity vectors over 50 cm/s are misrepresented as negative velocities travelling towards the heart for low-VENC at this thoracic plane during systole. At 900 ms (bottom row), high-VENC is incapable of distinguishing the fluid domain from static tissue in the abdominal plane (indicated in blue), while the low-VENC accurately represents the flow field and aortic lumen boundary.

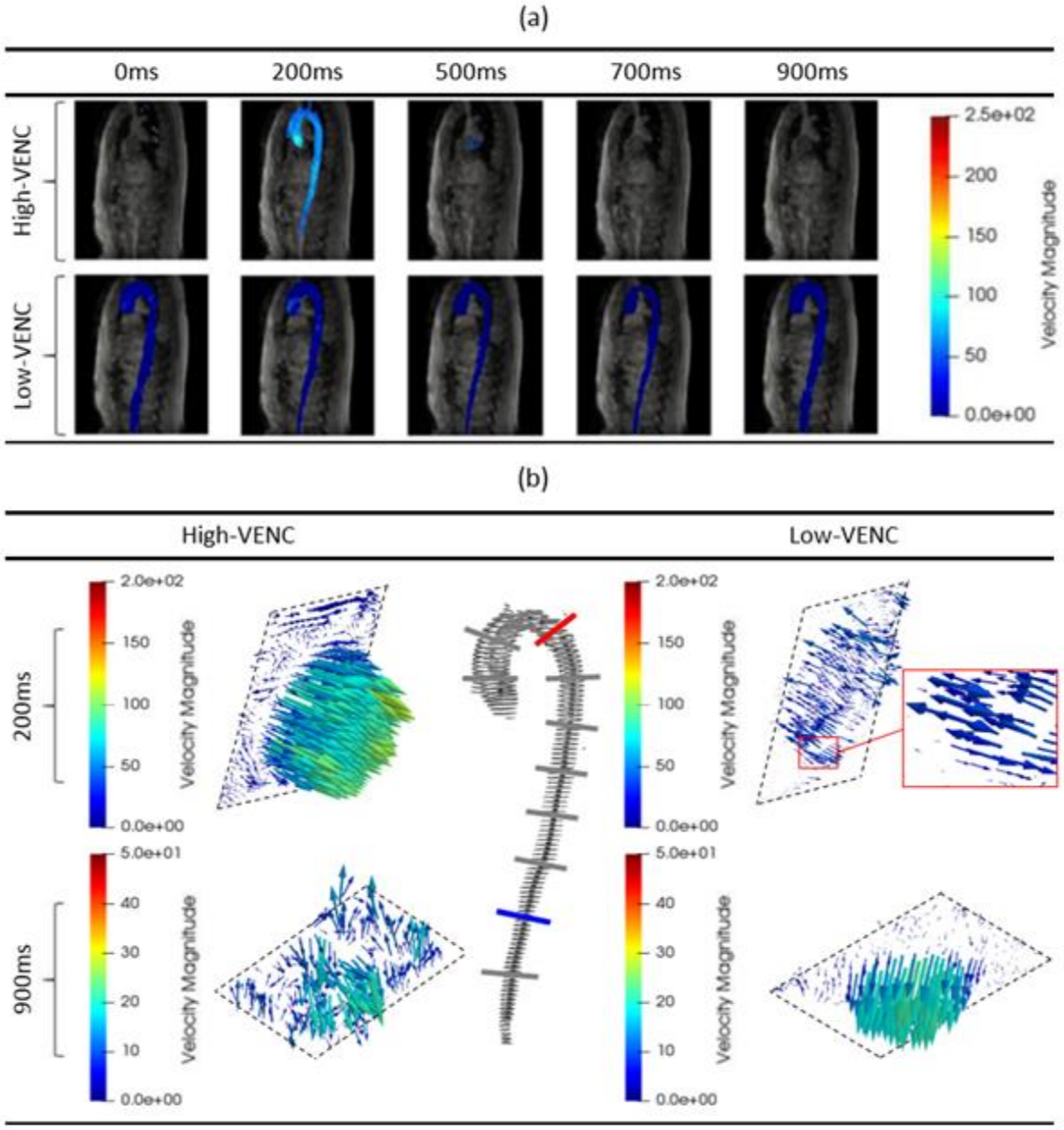

Figure 5: (a) Sagittal view of velocity magnitude vectors. The high-VENC (top row) captures systole, as shown at the 200 ms time-point. However, during diastole, low-velocity blood flow is not distinguishable from surrounding static tissue. The low-VENC provides accurate data on the region of blood-flow (and thus the lumen boundary) throughout the entire cardiac cycle. However, velocity aliasing is evident in low-VENC during systole. (b) Further emphasis of the requirement for dual-VENC approach, where top row indicates systole (200ms) in the thoracic plane (red), where high-VENC accurately illustrates the flow profile but velocity aliasing is evident in low-VENC (vectors above 50 cm/s travelling towards the heart). The bottom row illustrates how high-VENC cannot distinguish low velocity vectors from static tissue clearly in the abdominal plane (blue), while low-VENC can. By combining both data-sets in our dual-VENC approach, we obtain accurate measurements of the region of flow (and thus the lumen boundary) in addition to accurate measurement of the velocity vectors throughout the entire R-R interval in the entire aorta.

3.2 Spatial deformation

Figure 6 shows the spatial and temporal change in lumen cross-sectional-area throughout a cardiac cycle. Clearly the lumen cross-section-area (CSA) decreases with increasing distance from the heart at any given time-point in the cardiac cycle. For example, at time t=250 ms, the CSA at Plane 2 in the ascending aorta is 644 mm^2, compared to 295 mm^2 at Plane 5 and 158 mm^2 at Plane 10.

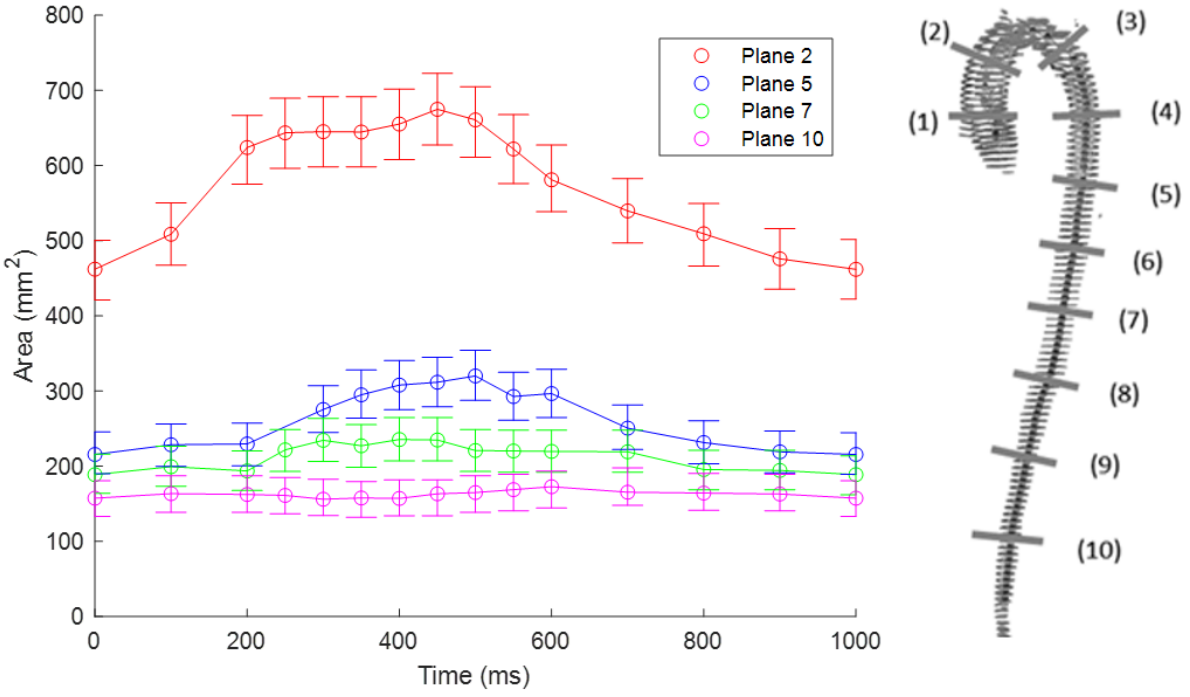

Figure 5: Area as a function of cardiac cycle time for a series of discrete planes along the vessel from proximal to distal aorta. Dashed lines represent errors pertaining to deformations smaller than the in-plane pixel resolution and therefore are not registered.

Figure 7(a) shows the lumen area at the end of diastole, A_{dia}, for all 10 planes. The well-known tapering of the aorta is also evident, with a decrease in A_{dia} with increasing distance from the heart. The percentage change in cross-sectional-area, $\Delta\hat{A}$, due to the onset of the pressure pulse is presented for each plane in Figure 7(b), where $\Delta\hat{A} = (A_{sys} - A_{dia})/A_{dia}$. Firstly, it should be noted that $\Delta\hat{A}$ ranges from 15% for Plane 10 up to 65% for Plane 1, providing an indication of the extremely large deformation of the aortic wall during a cardiac cycle. Indeed, it should be noted that the circumferential strains in the aortic tissue will be significantly larger than the values of $\Delta\hat{A}$ reported, given that the undeformed reference area (at zero pressure) is significantly lower than A_{dia} (clearly the true undeformed reference area cannot be determined in a "live" aorta, so the measure $\Delta\hat{A}$ is instead presented here to demonstrate the high aortic deformations during a cardiac cycle). Categorising the planes into

two subgroups, namely '*thoracic*' and '*abdominal*', a statistically significant difference in $\Delta\hat{A}$ is observed between the two groups ($p<0.005$).

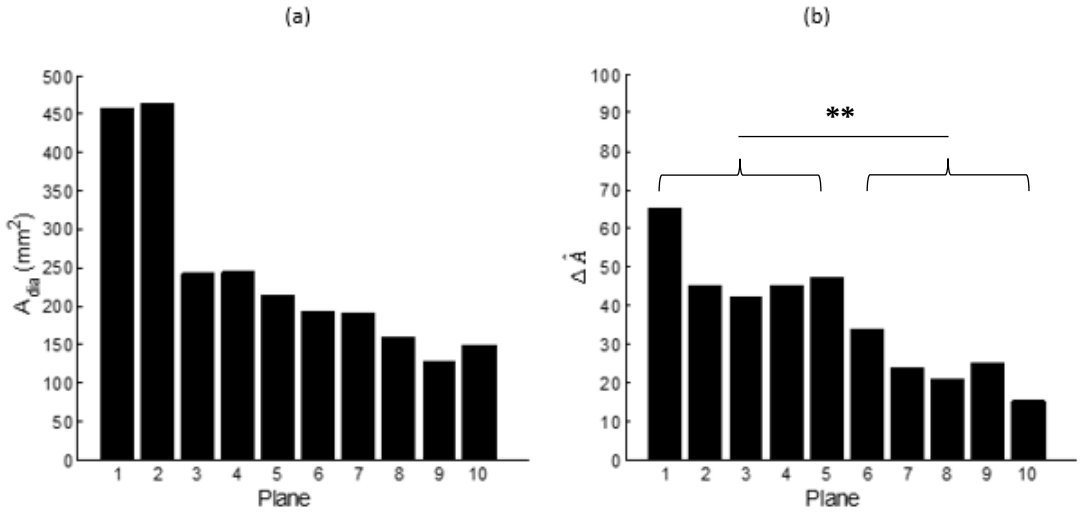

Figure 7: (a) Diastolic cross-sectional-area for each plane, highlighting the tapering of the aorta distally. (b) Cross-sectional-area change for each plane along the aorta. ** indicates a statistically significant difference between thoracic and abdominal aorta subgroups (p<0.005).

3.3 Spatial haemodynamics

The integral of the velocity matrix within the boundary of the fluid domain yields the volumetric flow rate, Q (Figure 8). The reduction of Q with increasing distance from the heart can be attributed, in part, to out-flow to visceral arteries including the supra-aortic, mesenteric and renal vessels. For example, the large drop in flow between Plane 1 and Plane 5 is associated with out-flow to the innominate, left common carotid, and left subclavian arteries supplying the head, neck, and upper body with a large volumetric blood flow. The opening of the aortic valve occurs at approximately 50 ms and closes at 500 ms, while the time lag between the flow peaks of each plane is related to the speed of the ejected pulse wave propagating through the aortic tree. Peak systolic blood flow ranges from 196 ml/s at Plane 1 in the ascending aorta to 28 ml/s at Plane 10 in the abdominal aorta, while diastolic flow at timepoint 600 ms ranges from 53ml/s at Plane 1 to 2ml/s in Plane 10. The non-zero flow during diastole, illustrates the well-known Windkessel effect. The measurements presented here demonstrate that the diastolic flow due to the Windkessel effect is highest in the ascending aorta and reduces with increasing distance from the heart.

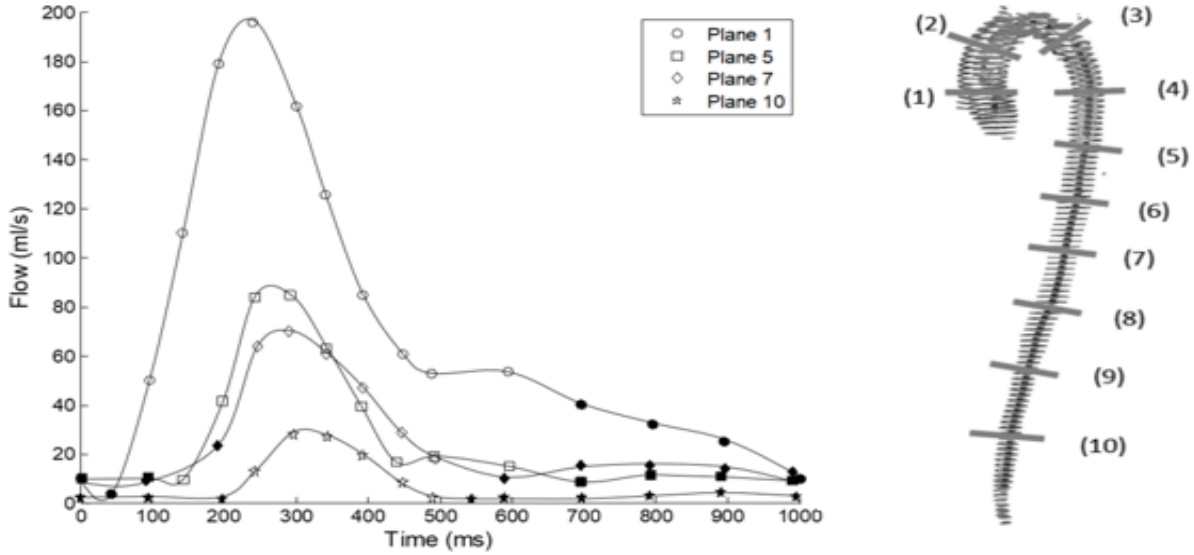

Figure 8: Aortic volumetric flow rate, Q throughout the cardiac cycle for a series of discrete planes along the vessel from proximal to distal aorta. Filled markers indicate phases where low-VENC was used and clear markers where high-VENC was used.

The coefficient of proportionality between Q and CSA provides the wave propagation speed (i.e. the speed of a blood column as it travels through the aorta following ventricular ejection), formally known as the pulse wave velocity (PWV). Figure 9(a) shows a higher wave velocity in the distal aorta than in the proximal aorta. Again, categorising the planes into two subgroups, *thoracic* and *abdominal*, a statistically significant difference in PWV between the two groups is found ($p<0.005$). The implementation of the TTP method to determine the PWV also provides a similar result, as shown in Figure 9(b); the PWV in the abdominal aorta (8.2 m/s) is found to be approximately 28% higher than in the thoracic aorta (6.4 m/s). The increased PWV in the abdominal aorta is due, in part, to the tapered geometry, as shown in Figure 7(a). However, spatial changes in vessel compliance also contribute to the observed increase in PWV.

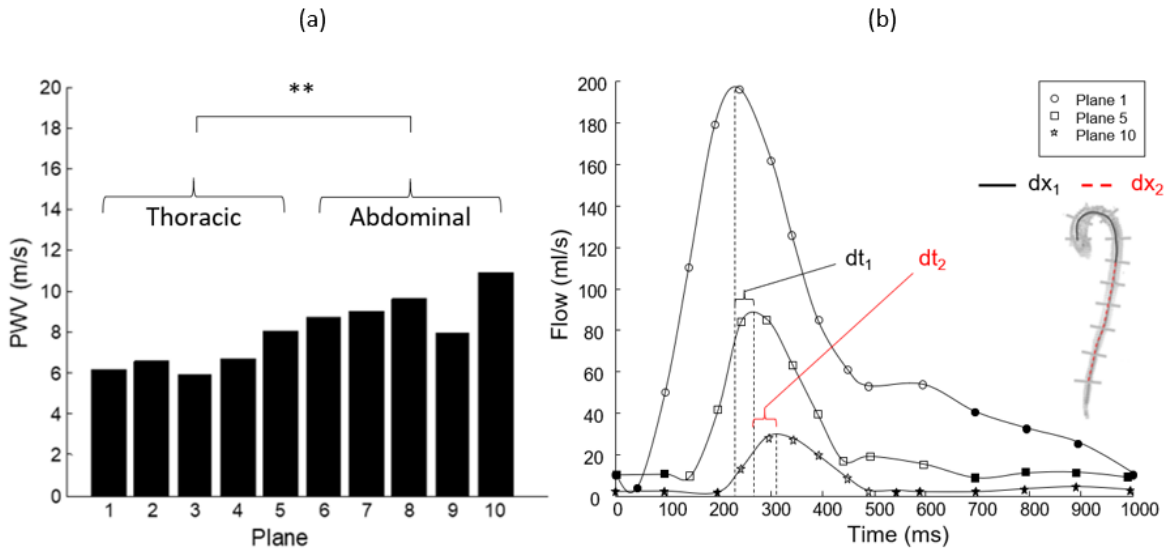

Figure 9: (a) PWV determined using the QA method. A gradient in wave speed is evident, increasing with distance from the heart. (b) PWV determined using the TTP method from Plane 1 to Plane 5 (thoracic) and Plane 5 to Plane 10 (abdominal). Thoracic and abdominal aortic segments exhibit a wave velocity of 6.36 m/s and 8.21 m/s respectively.

3.4 Spatial and temporal compliance

Spatial and temporal changes in vessel compliance are next investigated using the four blood pressure waveforms ((i) uniform brachial pressure wave, (ii) spatially varying pressure wave computed using the unsteady Bernoulli approach, (iii) spatially varying pressure wave determined using the piecewise approach, and (iv) spatially varying pressure wave computed by solving a full patient specific CFD analysis) determined in Section 2.5. In Figure 10, the instantaneous lumen cross-sectional-area is plotted as a function of blood pressure. Results are presented for the four aforementioned pressure waveforms at the proximal ascending aorta and the distal abdominal aorta. The instantaneous compliance at a given lumen pressure is given by the slope of the pressure-area graph. In all cases two distinct linear regions are observed, such that a high vessel compliance occurs at low pressures, and a low vessel compliance occurs at high pressures. The decrease in compliance at higher lumen pressures is due to strain stiffening constitutive behaviour of the aortic wall.

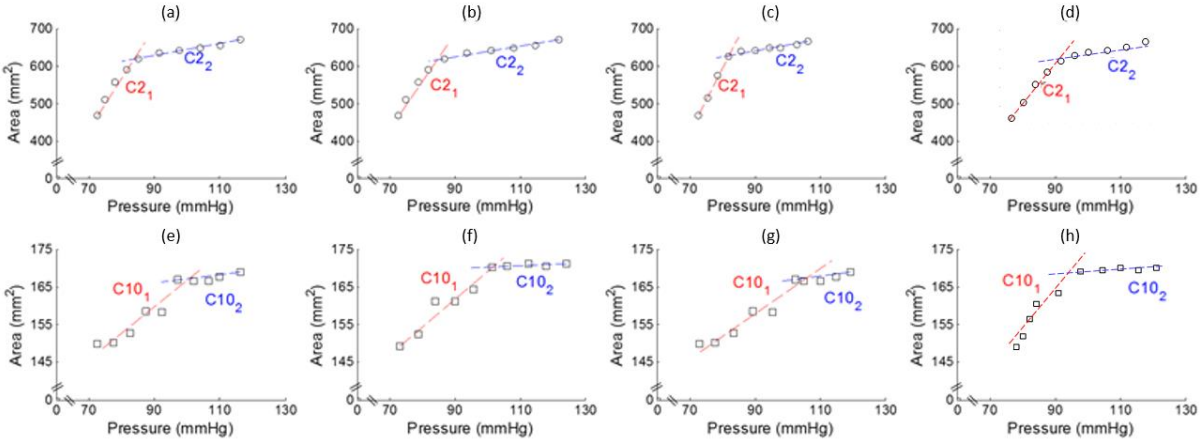

Figure 10: Area versus Pressure for the three pressure waveforms: (a,e) uniform aortic pressure wave; (b,f) spatially varying pressure wave computed using unsteady Bernoulli approach; (c,g) spatially varying pressure wave determined using piecewise approach; (d,h) spatially varying pressure wave determined by solving a full patient specific CFD analysis. Circular markers represent Plane 2 (proximal ascending thoracic aorta) and square markers represent Plane 10 (distal infrarenal abdominal aorta). Two-distinctive linear compliance regimes are evident in each case. The values of the bi-linear compliance are determined from the slope of the best-fit lines. High compliance regimes labelled with red lines and subscript "1", and low compliance regimes labelled with blue lines and subscripts "2"; e.g. $C10_2$ indicates the low compliance regime of plane 10. Results highlight a strong dependence of compliance on transient lumen pressure and on spatial location.

For each case presented in Figure 10, the value of compliance is determined using linear regression fits for the two distinct regions (red and blue) of the pressure-area graphs (values are presented in Table 1)**.** Clear evidence of strain stiffening is visible in each subplot of Figure 10, where significantly higher aortic dilation for a given change in pressure are observed in the high compliance (red) regime, compared to the low compliance (blue) regime. As an example, for Plane 2 (Figure 10(a) (uniform blood pressure waveform)) the compliance at low pressure ($C2_1$ = 11.94 mm^2/mmHg) is over eight times higher than the compliance at high pressure ($C2_2$ = 1.48 mm^2/mmHg). For Plane 2 the high compliance regime occurs for pressures below 85 mmHg. While a broadly similar bi-linear behaviour is also observed at Plane 10 (abdominal aorta), compliance values are an order of magnitude lower than those at Plane 2 (ascending aorta). As an example, for Plane 10 (Figure 10(d) (uniform blood pressure waveform)) a high compliance value of $C10_1$ = 0.67 mm^2/mmHg is determined, with a low compliance value of $C10_1$ = 0.11 mm^2/mmHg. Furthermore, at Plane 10 the change in compliance regime is observed to occur at a pressure of ~100 mmHg (compared to ~85 mmHg at Plane 2). These results highlight the dramatic differences in *in-vivo* material behaviour between the thoracic and abdominal aorta. Despite the fact that higher material strains occur in the thoracic aorta, as evident from Figure 7, the instantaneous

material stiffness is significantly higher in the abdominal aorta. The higher stiffness of the abdominal aorta explains, in part, the higher PWV in this region, as observed in Figure 9.

Figure 11 shows an approximation of the circumferential stress versus strain, derived from the area-pressure curves for the proximal ascending and distal abdominal aorta, based on the law of Laplace where P is pressure, r is the radius, and t is wall thickness. In each case significant strain stiffening is observed. It should be noted that these computed values do not consider the unloaded or stress-free reference configuration and are purely to demonstrate the significant stiffening observed throughout the cardiac cycle due to the straightening of collagen fibres. Follow on work has been conducted by the authors incorporating the zero-pressure equilibrium configuration with a novel physiologically motivated constitutive law to capture the non-linearity in a physical manner.

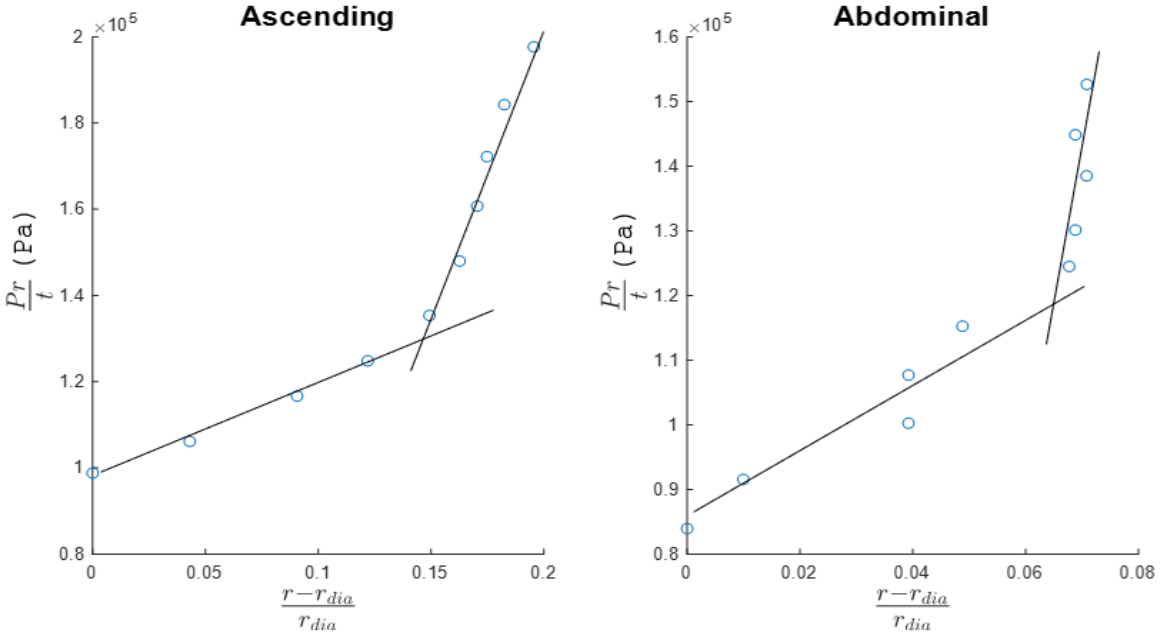

Figure 11: Approximation of circumferential stress versus strain plot derived from the area-pressure curves for the proximal ascending and distal abdominal aorta, based on the law of Laplace where P is pressure, and t is wall thickness, and the change in radius (r). It should be noted that these computed values do not consider the unloaded or stress-free reference configuration and are purely to demonstrate the significant stiffening observed throughout the cardiac cycle due to the straightening of collagen fibres. Follow on work has been conducted by the authors incorporating the zero-pressure equilibrium configuration with a novel physiologically motivated constitutive law to capture the non-linearity in a physical manner.

Table 1: Compliance values based on linear regression best-fits to the low and high compliance regime data presented in Figure 10. C2 represents Plane 2 and C10 Plane 10 with subscripts 1 and 2 representing high and low compliance regimes, respectively.

	Uniform		Bernoulli		Piecewise		CFD	
	C (mm^2/mmHg)	(R^2)	C (mm^2/mmHg)	(R^2)	C (mm^2/mmHg)	(R^2)	C (mm^2/mmHg)	(R^2)
$C2_1$	11.94	(0.973)	10.64	(0.961)	17.1	(0.998)	10.44	(0.985)
$C2_2$	1.48	(0.974)	1.32	(0.976)	1.40	(0.944)	1.62	(0.968)
$C10_1$	0.67	(0.892)	0.70	(0.933)	0.56	(0.919)	1.02	(0.839)
$C10_2$	0.11	(0.619)	0.04	(0.523)	0.12	(0.649)	0.03	(0.532)

4 Discussion

In this study a dual-VENC 4D Flow MRI protocol is developed to achieve accurate measurement of the dynamically changing flow velocity field and lumen area throughout the entire cardiac cycle and the entire aorta. To the best of our knowledge, no previous medical imaging paper has reported such detailed spatial and temporal characterisation of the human aorta. A nonlinear relationship between lumen area and pressure is observed *in-vivo* over the duration of a cardiac cycle throughout the entire aorta, suggesting that aortic biomechanics may not be accurately characterised by a single value compliance coefficient, as commonly assumed [32]–[34]. Furthermore, our detailed *in-vivo* measurements reveal that the lumen pressure-area relationship, and PWV are highly heterogeneous throughout the aorta.

4.1 Spatial deformation

We examine the deformation of the human aorta during the entire cardiac cycle at 10 planes, ranging from the sinus of Valsalva to immediately proximal to the common iliac bifurcation. The high levels of cross-sectional-area change, $\Delta\hat{A}$ during a cardiac cycle, ranging from 15% in the abdominal aorta to 65% in the ascending aorta, highlight the extremely large deformations of the aortic wall. The levels of deformation observed over a cardiac cycle are similar to those reported in previous studies. Sonesson et al., report a 20% increase in diameter in the abdominal aorta in young adults using ultrasound [68] (approx. 44% area increase), while [69]–[71] all report an increase in area of >100% in thoracic mice aortae. Accurate characterisation of such large deformations requires detailed imaging of the entire aorta throughout the entire cardiac cycle. While the observed trend that dilation reduces with distance from the heart is in broad agreement with previous non-invasive imaging studies by [14] and [72], the current study provides further insights by measuring dilation on a large number of planes spanning the entire aorta. A number of *ex-vivo* studies also suggest that compliance decreases with distance from the heart [12], [13]. A study by Tsamis and Vorp

[73] reports that the ascending thoracic aorta contains 80 elastin lamellar units while the infra-renal abdominal aorta contains 32. The decrease in elastin and increase in collagen observed by Concannon [74], provides a microstructural explanation for the decrease in compliance observed here with distance from the heart. Moreover, Tsamis and Vorp [73] also report a 50% decrease in elastin units between the descending thoracic and supra-celiac aorta, possibly providing an explanation for locally varying cross-sectional-area change observed in the current study. A review paper by Sherif [75] reports that the aorta, from a developmental point of view, is not a homogeneous structure nor one contiguous anatomical entity. Rather, it is suggested that the vessel can be split into discrete segments, each of which develops and differentiates under a distinct set of genetic and transcriptional factors. It is hypothesized that the regional differences in biomechanical behaviour may be due to the development of the ascending thoracic from neural crest cells and descending thoracic aorta from the mesoderm. With distinct connections or "weld points" between such segments, this may be the cause for local differences in cross-sectional-area change and PWV measured between adjacent planes in the current study.

4.2 Spatial haemodynamics

A notable outcome of this study is the spatial variance in PWV along the aorta. Results show that the PWV increases with increasing distance from the heart. This finding is reinforced using the TTP method, uncovering a 28% increase in PWV between the thoracic and abdominal aorta (6.4 m/s versus 8.2 m/s). Generally, PWV is defined in the literature as a single value for the aorta [9], [76]–[79]. The assumption of a uniform single valued PVW is primarily due to the method of clinical measurement, where the pressure pulse between two distinct sites, most commonly the carotid and femoral arteries (cfPWV) is recorded. The Reference Values for Arterial Stiffness' Collaboration [80], report a mean PWV value of 6.2 m/s for a cohort of 1455 normal subjects < 30 year of age. However, the pathway over which cfPWV is defined does not include the highly compliant ascending aorta. The utilization of MRI techniques to quantify aortic PWV has the ability to quantify changes at a local level, producing an accurate patient-specific spatial map of PVW. A study by Quinaglia [81] reported PWV readings targeted to the ascending aorta and found velocities of between 4 and 5.8 m/s, while [82] investigated the brachio-femoral pathway in 152 young adults and found mean PWV values of 8.7 m/s. Such measurements are comparable with the data presented in the current study for the thoracic and abdominal aorta respectively.

4.3 Spatial and temporal compliance

Compliance is generally presented as a single value, by taking the difference in area between diastole and systole and dividing this by patient's change in blood pressure. Aortic tissue is not a simple linear elastic material. Rather it exhibits a significant increase in stiffness when it is stretched to a high level of deformation [83]. Such mechanical behaviour occurs due to the structural contribution of collagen fibres. At low arterial strains collagen fibres are wavy, and an incremental increase in applied force will result in a significant increase in the length of the fibre, i.e. the fibre exhibits a low structural stiffness at low levels of deformation. A further incremental increase in force applied to a straightened collagen fibre will not result in a large increase in the length of the fibre. This is because the straightening of the fibre at high levels of deformation results in an increase of the structural stiffness [84].

The structural contribution of collagen results in the well-established non-linear stress-strain relationship for arterial tissue, whereby the material exhibits low stiffness at low strains and high stiffness at high strains. The transition from the low stiffness regime to the high stiffness regime is commonly modelled using exponential strain stiffening material laws [84], [85]. To date such models have been motivated and calibrated using *in-vitro* tests of excised arterial tissue. Our study provides evidence, that significant strain stiffening of the aorta occurs *in-vivo* over the deformation range of a cardiac cycle. This suggests that clinical compliance (defined as a change in lumen area with respect to a change in pressure) should not be characterised by a single value. Rather, a high compliance regime is observed for low pressures during diastole, followed by a transition to a low compliance regime for high pressures during systole. This *in-vivo* observation is consistent with strain stiffening observed in *in-vitro* testing, and it calls into question the accuracy of the common assumption that *in-vivo* lumen area increases linearly with lumen pressure during a cardiac cycle (inherent in the description of compliance by a single coefficient, e.g. [33], [86]–[91]).

Previous *in-vivo* analyses of the human aorta include an investigation of compliance in the abdominal segment using ultrasound [15], where the authors report a decrease in compliance with age, however such an imaging modality is impractical in portions of the thoracic aorta due to blind spots from bronchial air [92]. Mohiaddin and colleagues investigated aortic compliance using MRI in the thoracic segment in a large cohort of 70 volunteers [14], and found that compliance was highest in the ascending segment, however images were only acquired at diastole and systole, a temporal resolution too low to capture any non-linearities.

Our study quantifies the values of high and low compliance during a cardiac cycle, and demonstrates that these values, and the associated transition pressures, are spatially heterogeneous. Results show that the aorta exhibits a high compliance regime (HCR) at low pressures and a low compliance regime (LCR) at higher pressures, within each cardiac cycle. This non-linearity in compliance has been widely observed *in-vitro* whereby the instantaneous stiffness of arterial tissue increases with increasing uniaxial or biaxial stretch [93]–[99]. It is important to note when attempting to characterize aortic mechanical properties non-invasively, that the diastolic configuration extracted from *in-vivo* analyses is not the zero-pressure nor the stress-free configuration. Therefore, the fitting of *in-vivo* pressure-area data without consideration of the sub-physiological regime, will yield unphysical results. Follow-on work has been conducted by the authors, identifying an equilibrium vessel configuration at zero applied lumen pressure, which is observed to be critical step required in order to predict the key features of the pressure-area relationship observed *in-vivo*. The role of elastin pre-stretch on the lumen pressure at which the aorta transitions from a high compliance to a low compliance regime due to collagen strain stiffening, is also investigated using a novel physically based constitutive law. This modelling approach is also shown to capture the key features of elastin and SMC knockout experiments. Such detailed insights into vessel compliance are critical for development of an enhanced understanding of the relationship between pressure, blood flow, and PWV in the aorta, and will potentially lead to improved interventional procedures and device designs.

4.4 Limitations

A number of limitations should be noted for the current study, providing motivation for follow-on studies. The purpose of this study was to develop a dual-VENC imaging protocol to generate high resolution subject-specific data on heterogeneous non-linear aortic compliance and pulse wave velocity in a clinically feasible timeframe. While the data generated in the current study is limited to a single subject, the demonstration of this capability of our methodology provides a platform for extensive high-resolution characterisation of aortic biomechanics for populations of healthy and diseased subjects. It should be noted that increased temporal resolution, spatial resolution, coverage and signal to noise ratio all incur the cost of higher scan time and gradient coil capabilities in every MRI system. Hence, in order to maintain clinical feasibility temporal resolution was sacrificed in this study. In the ideal situation each phase would span a segment shorter than 50 ms, which may lead to greater accuracy in the quantification of area, flow and hence PWV, and so, more

work may be justified in this area to see if any further optimization of parameters is possible for imaging the aorta in its entirety, while maintaining a short scan time. Further improvements in spatial resolution may be possible with the clinical integration of 7T scanners, that may aid in the quantification of compliance in older stiffer aortae. It is expected that the compliance estimates obtained from the young healthy case would be higher than those of an older subject, due to the natural process of arteriosclerosis that occurs with age. Moreover, for older/sicker patients, faster more irregular cardiac cycles will increase scan time, which presents challenges in whether the MRI machine is capable of capturing, for example, 20 phases in a shortened irregular RR-interval. It should also be noted that this protocol can be readily applied to a 1.5T scanner, with the drawback of a significant time increase.

The same level of accuracy in area quantification cannot be achieved along the length of the aorta due to varying levels of compliance and a fixed spatial resolution, where deformations smaller than the pixel size are not registered. A possible solution to this exists in running a series of 2D PCMRI scans, with increasing in-plane resolution further from the heart, however such scans do not account for flow continuity between planes and extreme care should be taken to prescribe imaging planes orthogonal to the mean direction of flow at each location of interest.

In terms of determining aortic compliance, a challenge remains to accurately measure a continuous location-specific blood pressure waveform throughout the aorta without resorting to an invasive catheterization procedure. In the absence of a clearly defined best strategy to compute a continuous pressure waveform noninvasively [50], [100], we implemented four separate waveform generation methods, namely; ‘Uniform’, ‘Unsteady Bernoulli’, ‘Piecewise’, and ‘CFD’. In any case, the current study demonstrates that the bi-linearity of the measured compliance is not strongly affected by the method of approximating the lumen pressure waveform. Although there are differences in the slopes between each method, the bilinear nature of the pressure-area relationship is apparent in each case, and we rely on the goodness of fit to the data to provide the compliance estimates.

4.5 Implications

The results of this study have a number of potential implications for the fields of aortic biomechanics and cardiovascular surgery. The study presents a protocol that can provide accurate spatial and temporal measurements of compliance and PWV in the aorta. This may

provide an incremental step in understanding why cardiac events occur post-TEVAR, through a better understanding of the relationship between PWV, aortic stiffness and cardiac function. Stenting may have a spatially varying effect on the biomechanics of the aorta by inducing a cascade analogous to "*accelerated arteriosclerosis"* on the system. This in turn effects cardiac function, as documented elsewhere for arteriosclerosis developed during the ageing process [73], [101], [102]. During EVAR however, a significant reduction in compliance may occur instantaneously due to stent deployment, in contrast to arteriosclerosis, where compliance gradually reduces over a period of decades. A follow-on study by the authors demonstrates the importance of accurate characterization of non-linear aortic compliance and its implications on Nitinol stent-artery interactions. Simulations reveal that Nitinol stent-grafts stretch the artery wall so that collagen is stretched to a straightened high stiffness configuration. The high compliance regime (HCR) associated with low diastolic lumen pressure is eliminated, and the artery operates in the low compliance regime (LCR) throughout the entire cardiac cycle. The slope of the lumen pressure-area curve for the LCR post-implantation is almost identical to that of the native vessel during systole. This negligible change from the native systole slope occurs because the stent-graft increases its diameter from the crimped configuration during deployment so that it reaches a low stiffness unloading plateau (The effective radial stiffness of which is negligible compared to the stiffness of the artery wall). This highlights the need for accurate quantification of non-linear compliance in order to provide a mechanistic foundation for the common assumption that stents decrease aortic compliance [103]–[106]. The current study suggests that aortic compliance cannot be captured by a single value, and that the vessel is significantly less compliant in systole than diastole. Incorporating such detailed information into the design of EVAR devices with the aim of replicating the natural non-linear compliance of the vessel may reduce the prevalence of the aforementioned complications.

5 Conclusions

A dual-VENC 4D Flow MRI protocol is developed and implemented in a commercial scanner for characterising the biomechanics of the entire human aorta. A composite dataset approach is employed to maximally attenuate fluid contrast throughout the unsteady velocity profile of the cardiac cycle, providing an alternative method to phase unwrapping techniques. Pulse wave velocity increases from proximal to distal aorta, while cross-sectional-area change, volumetric flow rate and compliance all reduce with distance from the heart. Finally,

compliance is shown to alter significantly during the cardiac cycle, with significantly higher compliance being observed during periods of low blood pressure.

6 Acknowledgements

The author would like to acknowledge Mr. Torben Shneider and Mr. Matthew Clemence of Philips (Philips Medical Systems, Best, Netherlands) and Evelyn Smith and Marie McMullen (Department of Radiology, Galway Clinic) for their support and guidance during this study. This study was supported by the Irish Research Council (EPSPG_2016_194).

7 Disclosures

None

8 Bibliography

[1] L. G. Svensson and E. R. Rodriguez, "Aortic organ disease epidemic, and why do balloons pop?," *Circulation*, vol. 112, no. 8, pp. 1082–4, Aug. 2005.

[2] C. W. Hicks *et al.*, "Hospital-Level Factors Associated With Mortality After Endovascular and Open Abdominal Aortic Aneurysm Repair," *JAMA Surg.*, vol. 150, no. 7, p. 632, Jul. 2015.

[3] I. trial IMPROVE Trial Investigators *et al.*, "Endovascular or open repair strategy for ruptured abdominal aortic aneurysm: 30 day outcomes from IMPROVE randomised trial.," *BMJ*, vol. 348, p. f7661, Jan. 2014.

[4] R. Patel, M. J. Sweeting, J. T. Powell, and R. M. Greenhalgh, "Endovascular versus open repair of abdominal aortic aneurysm in 15-years' follow-up of the UK endovascular aneurysm repair trial 1 (EVAR trial 1): a randomised controlled trial," *Lancet*, vol. 388, no. 10058, pp. 2366–2374, Nov. 2016.

[5] C. M. Bhamidipati *et al.*, "Have thoracic endografting outcomes improved since US Food and Drug Administration approval?," *Ann. Thorac. Surg.*, vol. 91, no. 5, pp. 1314–22; discussion 1322, May 2011.

[6] M. F. Conrad, J. Tuchek, R. Freezor, J. Bavaria, R. White, and R. Fairman, "Results of the VALOR II trial of the Medtronic Valiant Thoracic Stent Graft," *J. Vasc. Surg.*, vol. 66, no. 2, pp. 335–342, Aug. 2017.

[7] M. S. Bischoff, M. Ante, K. Meisenbacher, and D. Böckler, "Outcome of thoracic endovascular aortic repair in patients with thoracic and thoracoabdominal aortic aneurysms," *J. Vasc. Surg.*, vol. 63, no. 5, pp. 1170-1181.e1, May 2016.

[8] J. Concannon, E. P. Kavanagh, N. Hynes, P. E. McHugh, J. P. McGarry, and S. Sultan, "The Streamliner Multilayer Flow Modulator in the treatment of Complex Thoracoabdominal Aortic Aneurysms," *Vascular*, vol. 25, no. 2_suppl, 2017.

[9] Y. Ben-Shlomo *et al.*, "Aortic Pulse Wave Velocity Improves Cardiovascular Event Prediction," *J. Am. Coll. Cardiol.*, vol. 63, no. 7, pp. 636–646, Feb. 2014.

[10] A. Dua, S. Kuy, C. J. Lee, G. R. Upchurch, and S. S. Desai, "Epidemiology of aortic

aneurysm repair in the United States from 2000 to 2010," *J. Vasc. Surg.*, vol. 59, no. 6, pp. 1512–1517, Jun. 2014.

[11] D. R. Nolan and J. P. McGarry, "On the correct interpretation of measured force and calculation of material stress in biaxial tests," *J. Mech. Behav. Biomed. Mater.*, vol. 53, pp. 187–199, Jan. 2016.

[12] T. Moriwaki *et al.*, "Variations in local elastic modulus along the length of the aorta as observed by use of a scanning haptic microscope (SHM)," *J. Artif. Organs*, vol. 14, no. 4, pp. 276–283, Dec. 2011.

[13] T. Krüger, K. Veseli, H. Lausberg, L. Vöhringer, W. Schneider, and C. Schlensak, "Regional and directional compliance of the healthy aorta: an ex vivo study in a porcine model," *Interact. Cardiovasc. Thorac. Surg.*, vol. 23, no. 1, pp. 104–111, Jul. 2016.

[14] R. H. Mohiaddin, S. R. Underwood, H. G. Bogren, D. N. Firmin, R. H. Klipstein, and D. B. Longmore, "Regional aortic compliance studied by magnetic resonance imaging: the effects of age, training, and coronary artery disease," *Br Hear. J*, vol. 62, pp. 90–6, 1989.

[15] T. Länne, B. Sonesson, D. Bergqvist, H. Bengtsson, and D. Gustafsson, "Diameter and compliance in the male human abdominal aorta: Influence of age and aortic aneurysm," *Eur. J. Vasc. Surg.*, vol. 6, no. 2, pp. 178–184, Mar. 1992.

[16] H. J. Kim *et al.*, "On Coupling a Lumped Parameter Heart Model and a Three-Dimensional Finite Element Aorta Model," *Ann. Biomed. Eng.*, vol. 37, no. 11, pp. 2153–2169, Nov. 2009.

[17] U. Morbiducci, R. Ponzini, D. Gallo, C. Bignardi, and G. Rizzo, "Inflow boundary conditions for image-based computational hemodynamics: impact of idealized versus measured velocity profiles in the human aorta.," *J. Biomech.*, vol. 46, no. 1, pp. 102–9, Jan. 2013.

[18] P. Crosetto, P. Reymond, S. Deparis, D. Kontaxakis, N. Stergiopulos, and A. Quarteroni, "Fluid–structure interaction simulation of aortic blood flow," *Comput. Fluids*, vol. 43, no. 1, pp. 46–57, Apr. 2011.

[19] J. R. Gohean, R. D. Moser, and Y. Zhang, "Patient-specific isogeometric fluid–structure interaction analysis of thoracic aortic blood flow due to implantation of the Jarvik 2000 left ventricular assist device," *Comput. Methods Appl. Mech. Eng.*, vol. 198, no. 45–46, pp. 3534–3550, Sep. 2009.

[20] M. Viceconti, A. Henney, and E. Morley-Fletcher, "In silico clinical trials: how computer simulation will transform the biomedical industry," *Int. J. Clin. Trials*, vol. 3, no. 2, p. 37, May 2016.

[21] H. Haraldsson *et al.*, "Assessment of Reynolds stress components and turbulent pressure loss using 4D flow MRI with extended motion encoding," *Magn. Reson. Med.*, vol. 79, no. 4, pp. 1962–1971, Apr. 2018.

[22] S. Petersson, P. Dyverfeldt, A. Sigfridsson, J. Lantz, C. J. Carlhäll, and T. Ebbers, "Quantification of turbulence and velocity in stenotic flow using spiral three-dimensional phase-contrast MRI," *Magn. Reson. Med.*, vol. 75, no. 3, pp. 1249–1255, Mar. 2016.

[23] A. A. Amini, A. Henn, S. Callahan, M. Kendrick, and A. Kheradvar, "An MR compatible aortic arch phantom with calcific polymeric valves," in *Medical Imaging 2019: Biomedical Applications in Molecular, Structural, and Functional Imaging*, 2019, vol. 10953, p. 55.

[24] S. Callahan *et al.*, "Dual-Venc acquisition for 4D flow MRI in aortic stenosis with spiral readouts," *J. Magn. Reson. Imaging*, p. jmri.27004, Dec. 2019.

[25] F. M. Callaghan *et al.*, "Use of multi-velocity encoding 4D flow MRI to improve quantification of flow patterns in the aorta," *J. Magn. Reson. Imaging*, vol. 43, no. 2, pp. 352–363, Feb. 2016.

[26] S. Schnell *et al.*, "K-t GRAPPA accelerated four-dimensional flow MRI in the aorta: Effect on scan time, image quality, and quantification of flow and wall shear stress," *Magn. Reson. Med.*, vol. 72, no. 2, pp. 522–533, Aug. 2014.

[27] H. Ha *et al.*, "Multi-VENC acquisition of four-dimensional phase-contrast MRI to improve precision of velocity field measurement," *Magn. Reson. Med.*, vol. 75, no. 5, pp. 1909–1919, May 2016.

[28] A. Nilsson, K. M. Bloch, M. Carlsson, E. Heiberg, and F. Ståhlberg, "Variable velocity encoding in a three-dimensional, three-directional phase contrast sequence: Evaluation in phantom and volunteers," *J. Magn. Reson. Imaging*, vol. 36, no. 6, pp. 1450–1459, Dec. 2012.

[29] C. Binter, V. Knobloch, R. Manka, A. Sigfridsson, and S. Kozerke, "Bayesian multipoint velocity encoding for concurrent flow and turbulence mapping," *Magn. Reson. Med.*, vol. 69, no. 5, pp. 1337–1345, May 2013.

[30] V. Knobloch *et al.*, "Mapping mean and fluctuating velocities by Bayesian multipoint MR velocity encoding-validation against 3D particle tracking velocimetry," *Magn. Reson. Med.*, vol. 71, no. 4, pp. 1405–1415, Apr. 2014.

[31] G. Sherrah, A, F. M. Callaghan, and S. M. Grieve, "Multi-Velocity Encoding Four-Dimensional Flow Magnetic Resonance Imaging in the Assessment of Chronic Aortic Dissection," *AORTA*, vol. 5, no. 3, pp. 80–90, 2017.

[32] Á. P. Tierney, A. Callanan, and T. M. McGloughlin, "In vivo feasibility case study for evaluating abdominal aortic aneurysm tissue properties and rupture potential using acoustic radiation force impulse imaging," *J. Mech. Behav. Biomed. Mater.*, vol. 4, no. 3, pp. 507–513, Apr. 2011.

[33] A. Lalande *et al.*, "Compliance and pulse wave velocity assessed by MRI detect early aortic impairment in young patients with mutation of the smooth muscle myosin heavy chain," *J. Magn. Reson. Imaging*, vol. 28, no. 5, pp. 1180–1187, Nov. 2008.

[34] T. Al Musa *et al.*, "Assessment of aortic stiffness by cardiovascular magnetic resonance following the treatment of severe aortic stenosis by TAVI and surgical AVR," *J. Cardiovasc. Magn. Reson.*, vol. 18, no. 1, p. 37, Dec. 2016.

[35] M. Cibis *et al.*, "Wall shear stress calculations based on 3D cine phase contrast MRI and computational fluid dynamics: A comparison study in healthy carotid arteries," *NMR Biomed.*, vol. 27, no. 7, pp. 826–834, 2014.

[36] W. V Potters *et al.*, "4D MRI-based wall shear stress quantification in the carotid bifurcation: a validation study in volunteers using computational fluid dynamics," *J.*

Cardiovasc. Magn. Reson., vol. 16, no. S1, Jan. 2014.

[37] M. Markl, A. Frydrychowicz, S. Kozerke, M. Hope, and O. Wieben, "4D flow MRI.," *J. Magn. Reson. Imaging*, vol. 36, no. 5, pp. 1015–36, Dec. 2012.

[38] Z. Stankovic, B. D. Allen, J. Garcia, K. B. Jarvis, and M. Markl, "4D flow imaging with MRI.," *Cardiovasc. Diagn. Ther.*, vol. 4, no. 2, pp. 173–92, Apr. 2014.

[39] M. Markl, S. Schnell, C. Wu, and C. . Rigsby, "Advanced flow MRI: emerging techniques and applications," *Clin. Radiol.*, 2016.

[40] H. Ha *et al.*, "Hemodynamic Measurement Using Four-Dimensional Phase-Contrast MRI: Quantification of Hemodynamic Parameters and Clinical Applications," *Korean J. Radiol.*, vol. 17, no. 4, p. 445, 2016.

[41] J. P. Ridgway, "Cardiovascular magnetic resonance physics for clinicians: part I," *J. Cardiovasc. Magn. Reson.*, vol. 12, no. 1, p. 71, Nov. 2010.

[42] J. D. Biglands, A. Radjenovic, and J. P. Ridgway, "Cardiovascular magnetic resonance physics for clinicians: part II," *J. Cardiovasc. Magn. Reson.*, vol. 14, no. 1, p. 66, Sep. 2012.

[43] M. A. Bernstein, K. F. King, and X. J. Zhou, *Handbook of MRI pulse sequences*. Academic Press, 2004.

[44] K. C. Tan, T. H. Kim, S. I. Chun, W. J. Shin, and C. W. Mun, "A Simple, Fast, and Robust Phase Unwrapping Method to Unwrap MR Phase Images," in *4th Kuala Lumpur International Conference on Biomedical Engineering 2008*, Berlin, Heidelberg: Springer Berlin Heidelberg, 2008, pp. 487–490.

[45] M. Loecher, E. Schrauben, K. M. Johnson, and O. Wieben, "Phase unwrapping in 4D MR flow with a 4D single-step laplacian algorithm," *J. Magn. Reson. Imaging*, vol. 43, no. 4, pp. 833–842, Apr. 2016.

[46] X. Su and W. Chen, "Reliability-guided phase unwrapping algorithm: a review," *Opt. Lasers Eng.*, vol. 42, no. 3, pp. 245–261, Sep. 2004.

[47] J. Cheng *et al.*, "A novel phase-unwrapping method based on pixel clustering and local surface fitting with application to Dixon water-fat MRI," *Magn. Reson. Med.*, vol. 79, no. 1, pp. 515–528, Jan. 2018.

[48] R. Cusack and N. Papadakis, "New Robust 3-D Phase Unwrapping Algorithms: Application to Magnetic Field Mapping and Undistorting Echoplanar Images," *Neuroimage*, vol. 16, no. 3, pp. 754–764, Jul. 2002.

[49] J. M. Bioucas-Dias and G. Valadao, "Phase Unwrapping via Graph Cuts," *IEEE Trans. Image Process.*, vol. 16, no. 3, pp. 698–709, Mar. 2007.

[50] P. Dyverfeldt *et al.*, "4D flow cardiovascular magnetic resonance consensus statement," *J. Cardiovasc. Magn. Reson.*, vol. 17, no. 1, p. 72, Dec. 2015.

[51] N. J. Pelc, M. A. Bernstein, A. Shimakawa, and G. H. Glover, "Encoding strategies for three-direction phase-contrast MR imaging of flow.," *J. Magn. Reson. Imaging*, vol. 1, no. 4, pp. 405–13, 1991.

[52] M. Bustamante, V. Gupta, C.-J. Carlhäll, and T. Ebbers, "Improving visualization of 4D flow cardiovascular magnetic resonance with four-dimensional angiographic data:

generation of a 4D phase-contrast magnetic resonance CardioAngiography (4D PC-MRCA)," *J. Cardiovasc. Magn. Reson.*, vol. 19, no. 1, p. 47, Dec. 2017.

[53] S. Vulliémoz, N. Stergiopulos, and R. Meuli, "Estimation of local aortic elastic properties with MRI," *Magn. Reson. Med.*, vol. 47, no. 4, pp. 649–654, Apr. 2002.

[54] A. L. Wentland, T. M. Grist, and O. Wieben, "Review of MRI-based measurements of pulse wave velocity: a biomarker of arterial stiffness.," *Cardiovasc. Diagn. Ther.*, vol. 4, no. 2, pp. 193–206, Apr. 2014.

[55] A. Lalande *et al.*, "Compliance and pulse wave velocity assessed by MRI detect early aortic impairment in young patients with mutation of the smooth muscle myosin heavy chain," *J. Magn. Reson. Imaging*, vol. 28, no. 5, pp. 1180–1187, Nov. 2008.

[56] J. L. Cavalcante, J. A. C. Lima, A. Redheuil, and M. H. Al-Mallah, "Aortic Stiffness," *J. Am. Coll. Cardiol.*, vol. 57, no. 14, pp. 1511–1522, Apr. 2011.

[57] J. Zhou and Y. C. Fung, "The degree of nonlinearity and anisotropy of blood vessel elasticity," *Proc. Natl. Acad. Sci.*, vol. 94, no. 26, 1997.

[58] R. W. Ogden, "Nonlinear Elasticity, Anisotropy, Material Stability and Residual Stresses in Soft Tissue," in *Biomechanics of Soft Tissue in Cardiovascular Systems*, Vienna: Springer Vienna, 2003, pp. 65–108.

[59] V. Agrawal, S. A. Kollimada, A. G. Byju, and N. Gundiah, "Regional variations in the nonlinearity and anisotropy of bovine aortic elastin," *Biomech. Model. Mechanobiol.*, vol. 12, no. 6, pp. 1181–1194, Nov. 2013.

[60] P. Lamata *et al.*, "Aortic relative pressure components derived from four-dimensional flow cardiovascular magnetic resonance," *Magn. Reson. Med.*, vol. 72, no. 4, pp. 1162–1169, Oct. 2014.

[61] S. Vennin *et al.*, "Non-invasive calculation of the aortic blood pressure waveform from the flow velocity waveform: a proof of concept," *Am. J. Physiol. - Hear. Circ. Physiol.*, p. ajpheart.00152.2015, Jul. 2015.

[62] K. M. Moerman, "GIBBON: The Geometry and Image-Based Bioengineering add-On," *J. Open Source Softw.*, vol. 3, no. 22, p. 506, 2018.

[63] S. A. Maas, B. J. Ellis, G. A. Ateshian, and J. A. Weiss, "FEBio: Finite elements for biomechanics," *J. Biomech. Eng.*, vol. 134, no. 1, 2012.

[64] E. J. Nett *et al.*, "Four-dimensional phase contrast MRI with accelerated dual velocity encoding," *J. Magn. Reson. Imaging*, vol. 35, no. 6, pp. 1462–1471, Jun. 2012.

[65] R. Moersdorf *et al.*, "Precision, reproducibility and applicability of an undersampled multi-venc 4D flow MRI sequence for the assessment of cardiac hemodynamics," *Magn. Reson. Imaging*, vol. 61, pp. 73–82, Sep. 2019.

[66] D. Giese, J. Wong, G. F. Greil, M. Buehrer, T. Schaeffter, and S. Kozerke, "Towards highly accelerated Cartesian time-resolved 3D flow cardiovascular magnetic resonance in the clinical setting," *J. Cardiovasc. Magn. Reson.*, vol. 16, no. 1, p. 42, Jun. 2014.

[67] S. Schnell *et al.*, "Accelerated dual-venc 4D flow MRI for neurovascular applications," *J. Magn. Reson. Imaging*, vol. 46, no. 1, pp. 102–114, Jul. 2017.

[68] B. Sonesson, T. Länne, E. Vernersson, and F. Hansen, "Sex difference in the

mechanical properties of the abdominal aorta in human beings," *J. Vasc. Surg.*, vol. 20, no. 6, pp. 959–969, 1994.

[69] H. Sugitani *et al.*, "Alternative splicing and tissue-specific elastin misassembly act as biological modifiers of human elastin gene frameshift mutations associated with dominant cutis laxa.," *J. Biol. Chem.*, vol. 287, no. 26, pp. 22055–67, Jun. 2012.

[70] J. Ferruzzi, M. R. Bersi, and J. D. Humphrey, "Biomechanical phenotyping of central arteries in health and disease: advantages of and methods for murine models.," *Ann. Biomed. Eng.*, vol. 41, no. 7, pp. 1311–30, Jul. 2013.

[71] J. Kim, A. J. Cocciolone, M. C. Staiculescu, R. P. Mecham, and J. E. Wagenseil, "Captopril treatment during development alleviates mechanically induced aortic remodeling in newborn elastin knockout mice," *Biomech. Model. Mechanobiol.*, Jul. 2019.

[72] N. Saouti, J. T. Marcus, A. V. Noordegraaf, and N. Westerhof, "Aortic function quantified: the heart's essential cushion," *J. Appl. Physiol.*, vol. 113, no. 8, pp. 1285–1291, Oct. 2012.

[73] A. Tsamis, J. T. Krawiec, and D. A. Vorp, "Elastin and collagen fibre microstructure of the human aorta in ageing and disease: a review.," *J. R. Soc. Interface*, vol. 10, no. 83, p. 20121004, Jun. 2013.

[74] J. Concannon *et al.*, "Quantification of the regional bioarchitecture in the human aorta," *J. Anat.*, p. joa.13076, Sep. 2019.

[75] H. M. F. Sherif, "Heterogeneity in the Segmental Development of the Aortic Tree: Impact on Management of Genetically Triggered Aortic Aneurysms.," *Aorta (Stamford, Conn.)*, vol. 2, no. 5, pp. 186–95, Oct. 2014.

[76] B. J. McDonnell *et al.*, "The age-dependent association between aortic pulse wave velocity and telomere length," *J. Physiol.*, vol. 595, no. 5, pp. 1627–1635, Mar. 2017.

[77] P. W. Wilson *et al.*, "Prediction of coronary heart disease using risk factor categories.," *Circulation*, vol. 97, no. 18, pp. 1837–47, May 1998.

[78] C. M. McEniery, Yasmin, I. R. Hall, A. Qasem, I. B. Wilkinson, and J. R. Cockcroft, "Normal Vascular Aging: Differential Effects on Wave Reflection and Aortic Pulse Wave Velocity: The Anglo-Cardiff Collaborative Trial (ACCT)," *J. Am. Coll. Cardiol.*, vol. 46, no. 9, pp. 1753–1760, Nov. 2005.

[79] J. Blacher, R. Asmar, S. Djane, G. M. London, and M. E. Safar, "Aortic pulse wave velocity as a marker of cardiovascular risk in hypertensive patients.," *Hypertens. (Dallas, Tex. 1979)*, vol. 33, no. 5, pp. 1111–7, May 1999.

[80] Reference Values for Arterial Stiffness' Collaboration, "Determinants of pulse wave velocity in healthy people and in the presence of cardiovascular risk factors: 'establishing normal and reference values,'" *Eur. Heart J.*, vol. 31, no. 19, pp. 2338–2350, Oct. 2010.

[81] T. Quinaglia *et al.*, "Differential impact of local and regional aortic stiffness on left ventricular remodeling," *J. Hypertens.*, vol. 36, no. 3, pp. 552–559, Mar. 2018.

[82] H. Boardman *et al.*, "Aortic stiffness and blood pressure variability in young people," *J. Hypertens.*, vol. 35, no. 3, pp. 513–522, Mar. 2017.

[83] D. R. Nolan and J. P. McGarry, “On the Compressibility of Arterial Tissue,” *Ann. Biomed. Eng.*, vol. 44, no. 4, pp. 993–1007, Apr. 2016.

[84] G. A. Holzapfel, T. C. Gasser, and R. W. Ogden, “A New Constitutive Framework for Arterial Wall Mechanics and a Comparative Study of Material Models,” *J. Elast. Phys. Sci. solids*, vol. 61, no. 1–3, pp. 1–48, 2000.

[85] D. . Nolan, R. W. Ogden, M. Destrade, and J. P. McGarry, “A robust anisotropic hyperelastic formulation for the modelling of soft tissue,” *J. Mech. Behav. Biomed. Mater.*, 2014.

[86] E. D. Lehmann *et al.*, “Relation between number of cardiovascular risk factors/events and noninvasive Doppler ultrasound assessments of aortic compliance.,” *Hypertens. (Dallas, Tex. 1979)*, vol. 32, no. 3, pp. 565–9, Sep. 1998.

[87] H. G. Bogren *et al.*, “The function of the aorta in ischemic heart disease: A magnetic resonance and angiographic study of aortic compliance and blood flow patterns,” *Am. Heart J.*, vol. 118, no. 2, pp. 234–247, Aug. 1989.

[88] J. Mitéran, O. Bouchot, A. Cochet, and A. Lalande, “Automatic determination of aortic compliance based on MRI and adapted curvilinear detector,” *Biomed. Signal Process. Control*, vol. 40, pp. 295–311, Feb. 2018.

[89] J. A. van Herwaarden *et al.*, “Aortic Compliance Following EVAR and the Influence of Different Endografts: Determination Using Dynamic MRA,” *J. Endovasc. Ther.*, vol. 13, no. 3, pp. 406–414, Jun. 2006.

[90] C. V Ioannou *et al.*, “Left ventricular hypertrophy induced by reduced aortic compliance.,” *J. Vasc. Res.*, vol. 46, no. 5, pp. 417–25, 2009.

[91] M. Vyas *et al.*, “Augmentation Index and Central Aortic Stiffness in Middle-Aged to Elderly Individuals,” *Am. J. Hypertens.*, vol. 20, no. 6, pp. 642–647, Jun. 2007.

[92] R. R. Baliga *et al.*, “The role of imaging in aortic dissection and related syndromes,” *JACC: Cardiovascular Imaging*, vol. 7, no. 4. Elsevier Inc., pp. 406–424, 01-Apr-2014.

[93] J. P. Vande Geest, M. S. Sacks, and D. A. Vorp, “The effects of aneurysm on the biaxial mechanical behavior of human abdominal aorta.,” *J. Biomech.*, vol. 39, no. 7, pp. 1324–34, Jan. 2006.

[94] T. Matsumoto *et al.*, “Biaxial Tensile Properties of Thoracic Aortic Aneurysm Tissues,” *J. Biomech. Sci. Eng.*, vol. 4, no. 4, 2009.

[95] Z. Teng *et al.*, “Layer- and Direction-Specific Material Properties, Extreme Extensibility and Ultimate Material Strength of Human Abdominal Aorta and Aneurysm: A Uniaxial Extension Study,” *Ann. Biomed. Eng.*, vol. 43, no. 11, pp. 2745–2759, Nov. 2015.

[96] K. Laksari, D. Shahmirzadi, C. J. Acosta, and E. Konofagou, “Energy-based constitutive modelling of local material properties of canine aortas,” *J. R. Soc. Interface*, vol. 3, no. 9, p. 160365, 2016.

[97] C. Forsell, J. Roy, and T. C. Gasser, “The Quasi-Static Failure Properties of the Abdominal Aortic Aneurysm Wall Estimated by a Mixed Experimental-Numerical Approach,” *Ann. Biomed. Eng.*, 2013.

[98] N. Gundiah, A. R. Babu, and L. A. Pruitt, “Effects of elastase and collagenase on the nonlinearity and anisotropy of porcine aorta,” *Physiol. Meas.*, vol. 34, no. 12, pp. 1657–1673, Dec. 2013.

[99] C. Reeps *et al.*, “Measuring and modeling patient-specific distributions of material properties in abdominal aortic aneurysm wall.,” *Biomech. Model. Mechanobiol.*, vol. 12, no. 4, pp. 717–33, Aug. 2013.

[100] A. Adji and M. F. O’Rourke, “Central aortic pressure calibration,” *J. Hypertens.*, vol. 35, no. 4, pp. 893–894, Apr. 2017.

[101] J. C. Kohn, M. C. Lampi, and C. A. Reinhart-King, “Age-related vascular stiffening: causes and consequences.,” *Front. Genet.*, vol. 6, p. 112, 2015.

[102] P. Wohlfahrt, M. M. Redfield, V. Melenovsky, F. Lopez-Jimenez, R. J. Rodeheffer, and B. A. Borlaug, “Impact of chronic changes in arterial compliance and resistance on left ventricular ageing in humans.,” *Eur. J. Heart Fail.*, vol. 17, no. 1, pp. 27–34, Jan. 2015.

[103] M. Back, G. Kopchok, M. Mueller, D. Cavaye, C. Donayre, and R. A. White, “Changes in arterial wall compliance after endovascular stenting,” *J. Vasc. Surg.*, vol. 19, no. 5, pp. 905–911, 1994.

[104] H. Vernhet, R. Demaria, J. M. Juan, M. C. Oliva-Lauraire, J. P. Sénac, and M. Dauzat, “Changes in wall mechanics after endovascular stenting in the rabbit aorta: Comparison of three stent designs,” *Am. J. Roentgenol.*, vol. 176, no. 3, pp. 803–807, 2001.

[105] L. Morris, F. Stefanov, N. Hynes, E. B. Diethrich, and S. Sultan, “An Experimental Evaluation of Device/Arterial Wall Compliance Mismatch for Four Stent-Graft Devices and a Multi-layer Flow Modulator Device for the Treatment of Abdominal Aortic Aneurysms.,” *Eur. J. Vasc. Endovasc. Surg.*, vol. 51, no. 1, pp. 44–55, Jan. 2016.

[106] F. J. H. Nauta *et al.*, “Impact of thoracic endovascular aortic repair on radial strain in an ex vivo porcine model.,” *Eur. J. Cardiothorac. Surg.*, vol. 51, no. 4, pp. 783–789, 2017.